1002

ETUDE DE LA CRISTALLISATION ET DE SON EFFET SUR LE COMPORTEMENT A LA RUPTURE DE TROIS VERRES METALLIQUES Ni-Ti-B.

Version publiée de la thèse présentée à l'Institut de Métallurgie Structurale de l'Université de Neuchâtel

par

Nima MERK

Ingénieur-physicienne EPFL

IMPRIMATUR POUR LA THÈSE

Etude de la cristallisation et de son effet sur le comportement à la rupture de trois verres métalliques Ni-Ti-B

de Madame Nima Merk

UNIVERSITÉ DE NEUCHATEL

FACULTÉ DES SCIENCES

La Faculté des sciences de l'Université de Neuchâtel, sur le rapport des membres du jury,

MM. les professeurs D.G. Morris, W. Form, A.L. Greer (Cambridge), W. Benoît (EPF-Lausanne) et J.L. Martin (EPF-Lausanne)

autorise l'impression de la présente thèse.

Neuchâtel, le 25 juin 1987

Le doyen:

François Sigrist

Acta metall. Vol. 35, No. 9, pp. 2213–2225, 1987
Printed in Great Britain.

0001-6160/87 $3.00 + 0.00

CRYSTALLIZATION PROCESSES IN Ni–Ti–B GLASSY ALLOYS OF NEAR-TERNARY-EUTECTIC COMPOSITION

N. MERK,[1] D. G. MORRIS[1] and P. STADELMANN[2]

[1]Institut de Métallurgie Structurale, Université de Neuchâtel, Switzerland and
[2]Institut Interdépartemental de Microscopie Electronique, Ecole Polytechnique, Lausanne, Switzerland

(*Received* 20 *September* 1986; *in revised form* 26 *January* 1987)

Abstract—The crystallization kinetics and mechanisms of three Ni–Ti–B glasses have been examined with a view to elucidating the roles of chemical composition and quenched structure on subsequent behaviour. Alloys of composition near a ternary-eutectic point have been chosen because they represent a real and complex situation where several crystalline phases may form simultaneously. Crystallization processes are analysed in terms of nucleation and growth stages. Different nucleation mechanisms have been observed for the different alloys: these seem to be best explained in terms of the detailed, short range ordered structure of the quenched glass. Analysis of crystal glass interface energies, based on structural examination using High Resolution Electron microscopy, indicates that it is not this energy term which controls the nucleation of crystals on annealing the glass. Crystal growth may involve a eutectic mechanism, or a single-phase mechanism controlled by interface or matrix-diffusion kinetics. Crystallization is fastest when eutectic nucleation and growth occurs: formation of the eutectic colony requires a specific sequence of phase nucleation, namely the initial formation of the phase of complex structure followed by the phase of simpler structure.

Résumé—Nous avons examiné la cinétique et les mécanismes de cristallisation de trois verres Ni–Ti–B dans l'intention d'élucider les rôles de la composition chimique et de la structure obtenue par trempe sur le comportement ultérieur. Nous avons choisi des alliages de composition voisine du point eutectique ternaire parce qu'ils représentent une situation réelle et complexe où plusieurs formes cristallines peuvent se former simultanément. Nous analysons les processus de cristallisation à partir des étapes de germination et de croissance. Nous avons observé pour les différents alliages différents mécanismes de germination dont la meilleure explication semble être la structure ordonnée à courte distance du verre trempé. L'analyse des énergies interfaciales cristal/verre, basée sur une étude structurale par microscopie électronique à haute résolution, montre que ce n'est pas ce terme d'énergie qui contrôle la germination des cristaux lorsque le verre est recuit. La croissance cristalline peut faire intervenir un mécanisme d'eutectique, ou un mécanisme de phase unique, contrôlé par la cinétique de diffusion dans la matrice ou à l'interface. La cristallisation est la plus rapide quand la germination et la croissance de l'eutectique interviennent: la formation de la colonie eutectique nécessite une séquence spécifique de germination de phase, à savoir la formation initiale de la phase de structure complexe suivie par la phase de structure plus simple.

Zusammenfassung—Kristallisationskinetik und-mechanismen von drei Ni–Ti–B-Gläsern wurden im Hinblick auf die Rolle der chemischen Zusammensetzung und der eingeschreckten Struktur bei dem nachfolgenden Verhalten untersucht. Es wurden Legierungen mit einer Zusammensetzung in der Nähe des ternären eutektischen Punktes ausgewählt; diese stellen eine reale und komplexe Situation dar, in der sich mehrere kristalline Phasen gleichzeitig bilden können. Die Kristallisationsprozesse werden im Zustand der Keimbildung und des Wachstums analysiert. In den verschiedenen Legierungen wurden unterschiedliche Keimbildungsmechanismen aufgefunden; diese scheinen sich am besten anhand der Nahordnungsstruktur des abgeschreckten Glases erklären zu lassen. Die Analyse der Energien der Kristall/Glas-Grenzflächen mittels hochauflösender Elektronenmikroskopie weist darauf hin, daß dieser Energieterm die Keimbildung von Kristallen bei der Wärmebehandlung des Glases nicht bestimmt. Das Kristallwachstum kann einen eutektischen Mechanismus enthalten, oder einen Einphasen Mechanismus, der durch die Kinetik der Grenzflächen-oder Matrixdiffusion gesteuert wird. Die Kristallisation läuft am schnellstenn ab, wenn eutektische Keimbildung und Wachstum auftreten. Die Bildung der eutektischen Kolonie erfordert einen speziellen Ablauf der Phasen-Keimbildung, nämlich die Bildung der Phase mit komplexer Struktur am Anfang, danach die Phase mit der einfacheren Struktur.

1. INTRODUCTION

Easy metallic glass formability is often found at compositions close to those of eutectics [1]. In addition, alloys containing several elements, that is not simple binary alloys, have extended glass-forming composition ranges. Accordingly it should not be uncommon for several crystalline phases to form, almost simultaneously, during crystallization. In fact the majority of crystallization studies has dealt with single-phase or single-eutectic transformations [2] and studies where more than two phases or two stages to crystallization have been observed are rare [3]. One of the major objectives of the present study has been to identify the factors controlling the rates of formation of the several competitive phases found during the crystallization of ternary–eutectic alloys.

Crystallization of glassy metals has been analysed in terms of nucleation and growth processes [2, 4]. The nucleation process may be unnecessary when

Table 1. Compositions of alloys studies (at. %)

Alloy Number	Nickel	Titanium	Boron
1	79.1	3.0	17.9
2	78.8	2.1	19.1
3	78.0	3.8	18.2

quenched-in crystals are present after glass preparation. Otherwise nucleation is often found to be an apparently homogeneous process and the classical homogeneous nucleation model used for analysis [5, 6]. On other occasions the presence of short range chemical order, or well-defined clusters of atoms, within the quenched glass has been invoked to explain the formation of specific crystalline species [7]. Formation of stable crystalline nuclei by homogeneous nucleation will depend strongly on the glass–crystal interface energy and according to Spaepen [8, 9] this can be largely interpreted in terms of the entropy charge at the interface. On the other hand, on the basis of the short range order model, nucleation will be less sensitive to the structure of the glass-crystal interface and presumably more dependent on the precise alloy composition.

The present study has combined the analysis of the crystallization mechanisms of several near-ternary–eutectic glassy alloys, including particular attention to the nucleation mechanisms, with the detailed study of the structure of glass-crystal interfaces using High Resolution Electron Microscopy.

2. EXPERIMENTAL

The alloys used for study were ternary Ni–Ti–B alloys. The detailed compositions are given in Table 1, and the alloys are placed in the context of the Ni–Ti–B ternary diagram [10] in Fig. 1. The alloys were chosen because of the possibility to obtain several crystalline phases by slight changes of chemical composition. These phases should have different mechanical properties and lead to different responses of the alloys during crystallization: a subsequent report will describe the mechanical responses observed.

The alloys were prepared by melt spinning (courtesy of Professor H.-J. Güntherodt, University of Basle) as ribbons about 9 mm wide and 20–25 μm thick. Heat treatments were performed in salt baths or in furnaces under argon atmosphere. The range of crystallization temperature for study was first estimated using a DSC-4 Differential Scanning Calorimeter operated at a heating rate of 40°C/min. Microstructural studies were carried out by transmission electron microscopy on thin foils prepared from the annealed ribbons. For these studies a Hitachi H-700 TEM operating at 200 kV was used. Thin foils were prepared by electropolishing in a Tenupol twin-jet polisher using a 10% perchloric acid–methanol mixture.

Crystal sizes and numbers were estimated using standard quantitative metallographic methods. The maximum crystal size corresponding to each alloy and heat treatment was determined by careful examination over several foils, each possessing a large transparent area. This method of crystal size measurement has been shown to be preferable for the evaluation of crystal growth kinetics [3, 11]. The number of crystals per unit volume was calculated [12] using

$$N_v = N_A/(t + D) \quad (1)$$

where N_A is the number of crystals per unit area, t the foil thickness and D the average crystal size. The foil thickness was initially measured by the stereographic examination of foil-surface artifacts, and subsequent studies performed on foil areas using the same screen intensity and beam focalisation conditions: the foil thickness was considered to be 0.3 μm throughout the entire study. The volume fraction of crystallized material was determined as

$$f_v = f_A/(1 + 3\,t/2\,D) \quad (2)$$

where f_A is the area fraction of crystallized material on the micrograph. The measured values of crystal size, crystal number and volume fraction are generally considered to be correct to $\pm 25\%$. At lower temperatures, particularly at the beginning of crystallization, the structure often appeared less uniform, and the error band should be increased to $\pm 40\%$. Towards the end of crystallization, for example after more than 60–80% transformation, it became difficult to allow for the effect of crystal overlap within the foil on the image obtained and the error band should also be considered as $\pm 40\%$.

High resolution electron microscopy was carried out using a Philips 430 ST microscope operated at 300 kV on newly-prepared foils. The point-to-point resolution of this microscope is better than 0.2 nm. Images were obtained without using an objective aperture, using axial illumination, and at an underfocus of 50–60 nm (Scherzer conditions). Best images of atom columns were obtained using a foil thickness

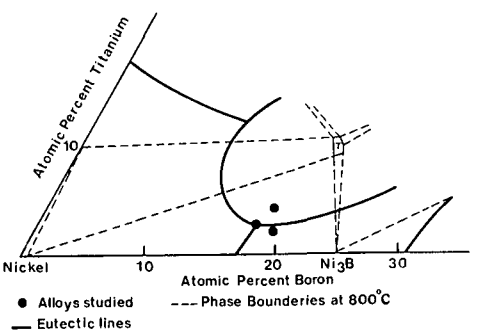

Fig. 1. The nickel corner of the nickel–titanium–boron equilibrium diagram [10] showing the equilibrium-phase regions at room temperature, the eutectic trenches, and the compositions of the alloys studied.

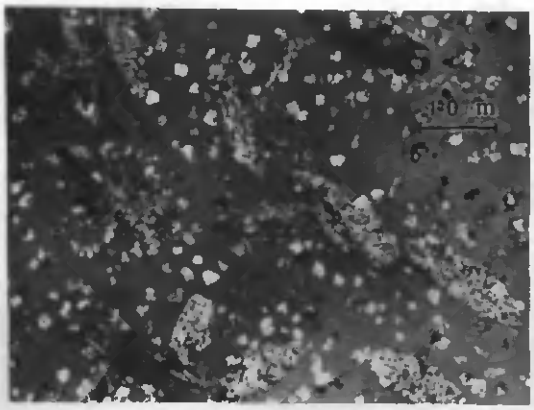

Fig. 2. Typical morphology of crystals in glassy Ni–3Ti–17.9B after annealing for 8 h at 300°C. Large eutectic colonies and small single-phase crystals are present.

of 7–10 nm. Photographs were recorded using a microscope magnification of ×700,000.

3. RESULTS

3.1. Alloy 1 (nickel–3% titanium–17.9% boron)

3.1.1. General morphology. This alloy has a composition close to that of the ternary eutectic, and under equilibrium cooling conditions would be expected to crystallize by the simultaneous formation of three phases, the orthorhombic Ni_3B (0 boride) complex face centre cubic, $(NiTi)_{23}B_6$ (τ phase), and face centre cubic nickel (γ Ni). By scanning calorimetry [heating rate 40°C/min] the crystallization temperature was established as 378°C and accordingly annealing temperatures of 260, 300 and 350°C were selected for isothermal annealing studies.

The typical morphology of the partially-crystallized material is shown in Fig. 2. Large eutectic colonies and a larger number of smaller crystals can be distinguished. The alloy continues to completion of crystallization with no change of morphology or crystal species. The smaller crystals were in fact of two types: an irregularly-shaped polycrystalline phase, Fig. 3(a), and a single-crystalline, faceted phase, Fig. 3(b). These crystals were identified by micro-diffraction as the γ Ni and the τ phase, respectively. Further corroboration was obtained by EDX analysis which showed that the γ Ni phase was very poor in titanium (it is difficult to obtain a precise measurement since the titanium content was extremely low, and scattered X-rays from the matrix inevitably led to some characteristic X-ray background) and the τ phase was considerably richer in titanium than the glass. It was not possible to determine the boron content using EDX. The large oval eutectic colonies were confirmed to contain both γ nickel and the orthorhombic Ni_3B phase. No conclusive evidence of τ phase was found within these eutectic colonies: it must be emphasized that the similarity in planar spacings for many of the crystal

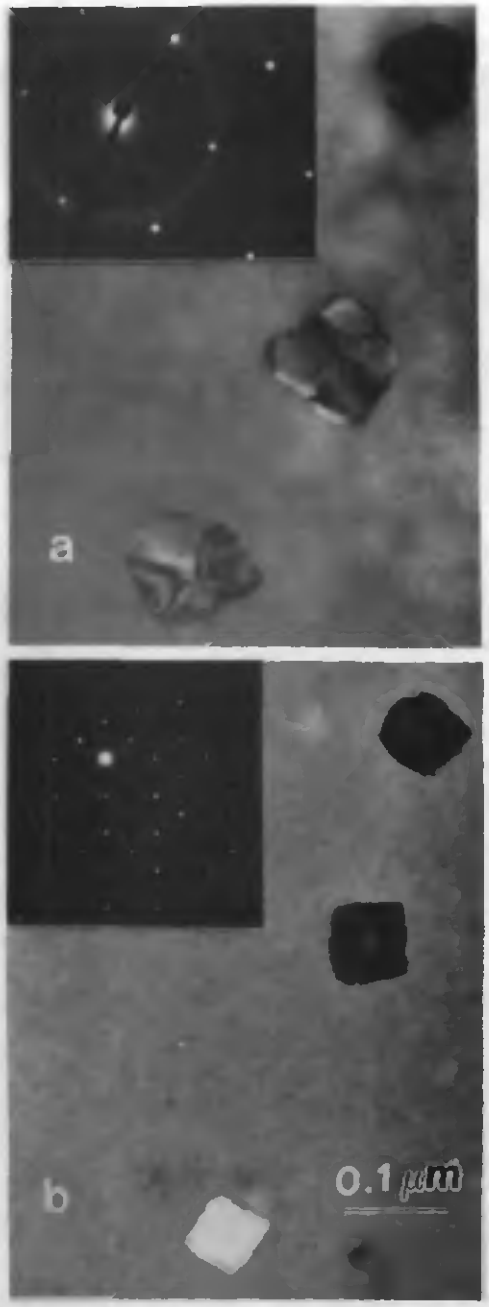

Fig. 3. Detailed views of the smaller phases found on crystallizing alloy 1: after annealing for 200 h at 260°C. (a) Polycrystalline aggregates of f.c.c. nickel; (b) facetted single crystals of the complex cubic boride (τ phase).

planes of the 0 boride, the τ phase and γ Ni make such identification of possible minor quantities of τ phase extremely difficult.

The lamellar eutectic colonies, as well as the single phase particles showed a textured orientation distribution. It was, for example, possible to orient many of the τ phase particles into the same Bragg-reflecting orientation at the same time. The eutectic colonies appeared to have their long axes randomly oriented within the plane of the foil (also the plane of the

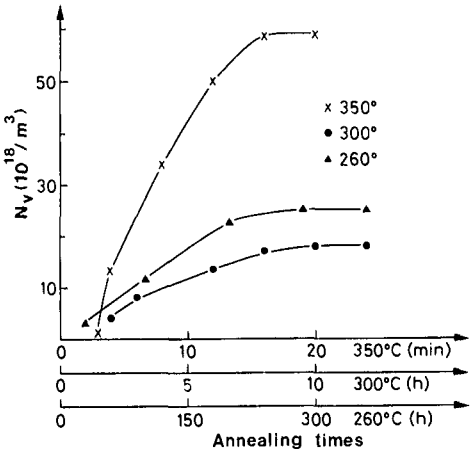

Fig. 4. The number of small crystals formed on annealing alloy 1 at each of the three temperatures.

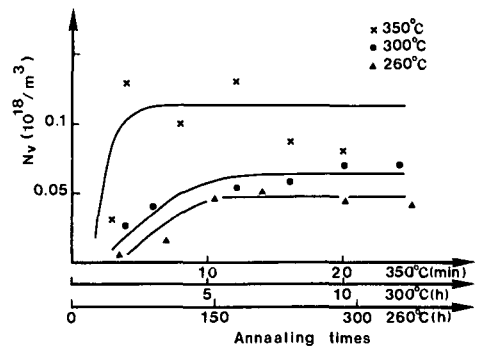

Fig. 5. The number of eutectic colonies formed on annealing alloy 1 at each annealing temperature.

ribbon) but none were found with the long axis significantly out of this plane.

3.1.2. Crystal nucleation. The variation in the number of small crystals and the number of eutectic colonies as a function of time at each temperature is shown in Figs 4 and 5 respectively. It should be emphasized that the majority of the small crystals are of the γ Ni phase, and in view of the difficulty of distinguishing between τ phase and γ Ni, the total number has been measured in each case. The measured kinetics of crystal nucleation can be taken to correspond to that of the γ Ni phase. At each temperature the number of crystals increases rapidly from zero (the fully amorphous state) at short annealing times and tends to saturate in number as full crystallization approaches. In view of the relatively large size of the crystals throughout esssentially all the crystallization process there are no major problems in detecting the crystals by TEM, and the variation in crystal number observed can only be explained by a nucleation process occurring on a fixed site number—an activated, nucleation process on some quenched-in structural inhomogeneity. For the three temperatures investigated, the maximum density of small crystals attained appears to have its lowest value at 300°C. The reason for this is not clear, but may be the result of a balance between changes in nickel nucleation rate and τ phase nucleation rate (at high temperatures the small crystals were almost uniquely nickel, while at low temperatures more τ phase was present), or changes in the amount of eutectic forming: as will be shown later the activation energies for nucleation and growth of the nickel phase and eutectic are not identical, and the relative amounts of nickel and eutectic phase are clearly temperature dependent.

The variation in the number of eutectic colonies with time at 260 and 300°C is of the same type as seen for the nickel, namely on initial rapid nucleation and a later saturation. The nucleation rate at 350°C appears to be so rapid that nucleation stops already after very short times.

According to the model of activated nucleation on a fixed number of quenched-in embryos, the number of crystals (N_t) present at time t can be described by

$$N_\infty - N_t = N_\infty \exp(-kt) \qquad (3)$$

where N_∞ is the total number of crystals forming at the given temperature and k a nucleation rate constant. This equation describes very well the experimental data both for nickel crystals and for eutectic colony nucleation, see Fig. 6. For the nickel the variation of the nucleation rate constant with temperature was consistent with an activation energy of 210 kJ/mol. The data on eutectic colony nucleation was imprecise because: at 350°C nucleation is already completed after very short times; at 260°C nucleation is very slow and not sufficient to allow consistent measurement by transmission microscopy even near full crystallisation. The data indicated an activation energy for eutectic colony nucleation considerably higher, 275 kJ/mol.

The sequence of processes leading to the appearance of the eutectic colony is not immediately clear, since either the orthorhombic boride or the f.c.c. nickel may nucleate first, and the critical nucleation process may be either the first or the second phase

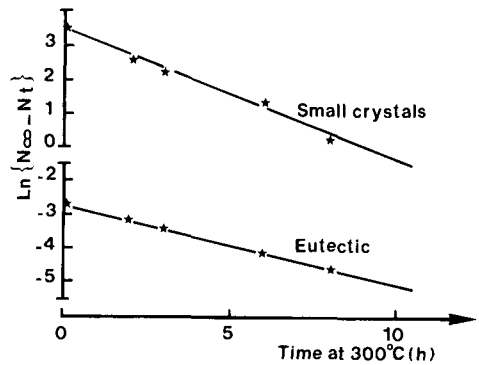

Fig. 6. Nucleation kinetics of nickel phase and eutectic colonies according to the model of nucleation on a fixed site density. Alloy 1, annealed at 300°C.

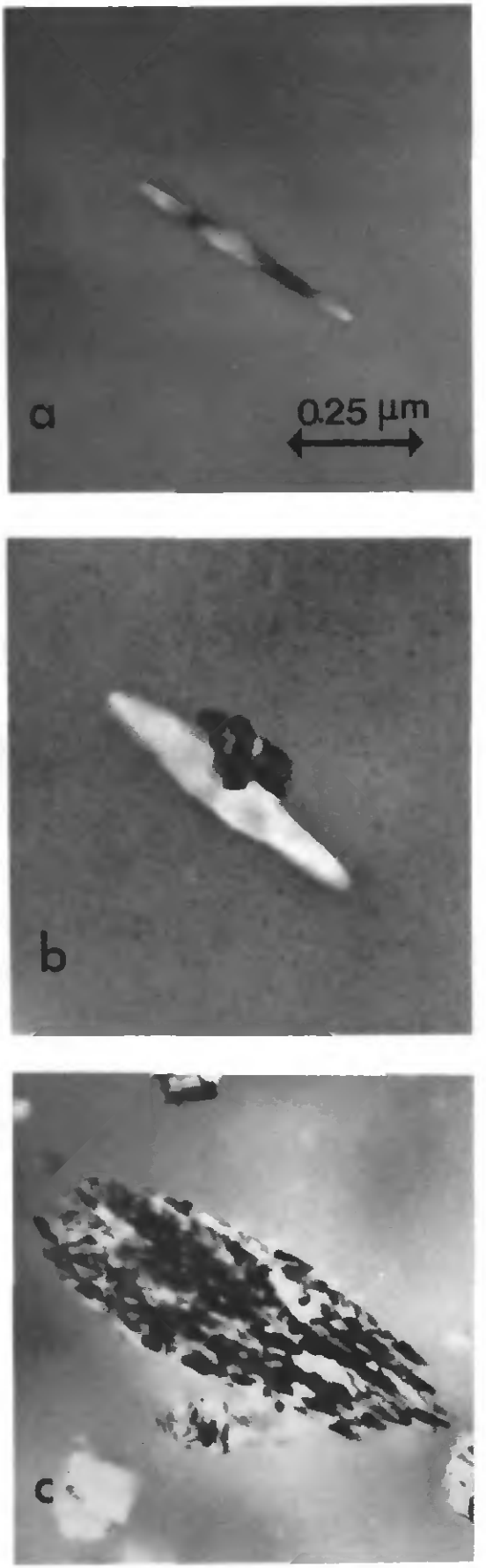

Fig. 7. Sequence of nucleation of the lamellar eutectic colony; annealing at 260°C: (a) isolated needle of orthorhombic boride; (b) single crystal nickel forms on the boride needle; (c) multiple-lamellar eutectic colony.

formation. Careful searching of a large number of foils revealed several just-nucleated eutectics [Fig. 7(b)] that is a single orthorhombic boride needle in contact with a single γ Ni crystal. A much smaller number of isolated, single-phase orthorhombic boride needles were found [Fig. 7(a)]. Such observations were made particularly at 260 and 300°C in view of the slower eutectic colony nucleation kinetics. In view of the relatively large number of γNi crystals which are present even after early crystallization, see for example Fig. 3, it is clearly impossible that these crystals could be the forerunners of eutectic colony nucleation. This is particularly evident at 350°C where τ phase and γNi nucleation continuous long after eutectic nucleation has finished. In consequence the sequence of eutectic formation can be taken as: boride needle formation [Fig. 7(a)] followed by γNi nucleation on the boride [Fig. 7(b)] and subsequent branching and growth leading to the large lamellar colonies [Fig. 7(c)].

3.1.3. Crystal growth. The crystal growth kinetics were examined by determining the largest crystal existing within a given material. This procedure for analysis requires a careful study of a large number of foils and a large sample volume, but is preferable to using an average crystal size because the value obtained is essentially independent of the kinetics of nucleation.

The growth of the small crystals (mostly nickel phase) is indicated in Fig. 8. At each temperature the crystals grow linearly with time. The data at 260°C may indicate that an initial rapid growth period is obtained. The variation in growth rate with temperature is described by an activation energy of 227 kJ/mol.

The growth of the lamellar eutectic colonies was also linear in time at each temperature, and about an order of magnitude larger than for the nickel, see Fig. 9. The data shown correspond to the maximum sizes of the long axes of the eutectic colonies. At each temperature and time the width of the eutectic colony was about one half to one third of its length. The variation in growth rate with temperature was consistent with an activation energy of 224 kJ/mol.

3.1.4. Overall crystallization kinetics. The overall crystallization kinetics for each of the three temperatures are given in Fig. 10. At each temperature the initial stages of crystallization have been examined in particular detail in order to allow an accurate determination of the transformation mechanisms.

3.2. Alloy 2 (nickel–2.1% titanium–19.1% boron)

3.2.1. General morphology. This alloy has a composition slightly closer to that of the orthorhombic

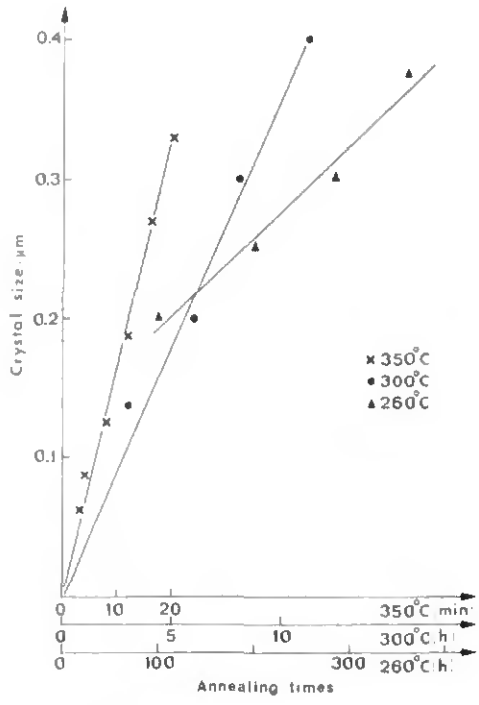

Fig. 8. Growth of the small (mostly nickel crystals) on annealing alloy 1.

boride. Scanning calorimetry [heating rate 40°C/min] indicates a crystallization temperature of 391°C and accordingly temperatures of 350, 300 and 280°C were selected for annealing studies.

The typical morphology of the partially crystallized alloy is shown in Fig. 11. Lamellar eutectic colonies, the same as observed for the alloy 1, are seen, lying once again predominantly in the plane of the foil. The phases present are the same, namely the orthorhombic boride and the nickel phase, and the sequence of nucleation is identical, namely first appearance of the boride needle, followed by appearance of the Nickel phase. The material continued to full crystallization in this way with no change in crystallization morphology. No sign of τ phase was found, although it must

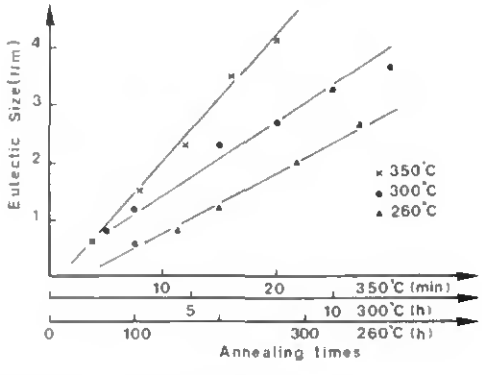

Fig. 9. Growth of the eutectic colonies on annealing alloy 1. The maximum size of the eutectic colony along its major axis is recorded in each case.

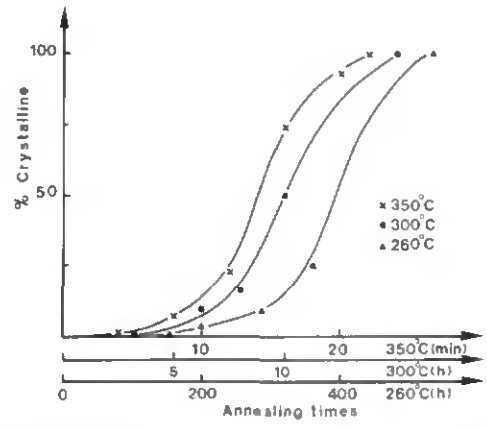

Fig. 10. Overall crystallization kinetics of alloy 1 at the three annealing temperatures.

again be emphasized that the similarity of planar spacings of many planes in the *O*-boride, the τ phase and the nickel make identification difficult.

3.2.2. Crystal nucleation. The variation in number of eutectic colonies on annealing is shown in Fig. 12. At each temperature the eutectic colonies appear over the first part of crystallization to reach a constant value after about 10% transformation. Thereafter the number of colonies remains essentially constant: the decrease recorded experimentally is believed to arise from the difficulty in allowing for overlap effects of the large and long colonies. The number of colonies produced is about the same for each temperature ($0.6/\mu m^3$) which is considerably more than obtained from the alloy 1 (up to $0.1/\mu m^3$ were observed). Based on the appearance of the eutectics over a considerable time period and the saturation in number after already a small fraction of crystallization, it is again considered that nucleation occurs on some quenched-in

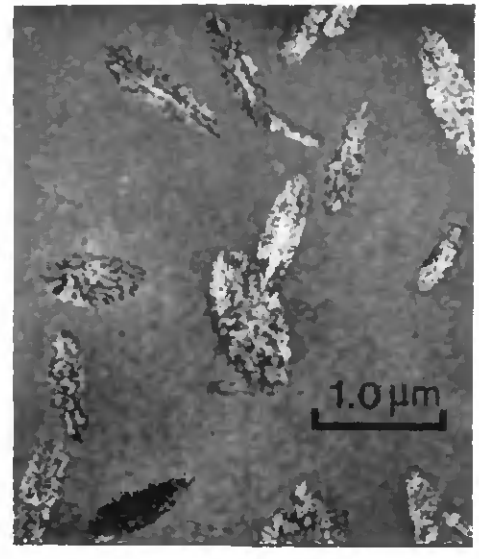

Fig. 11. Typical morphology of crystals formed on annealing alloy 2. Eutectic colonies of orthorhombic boride and nickel are seen.

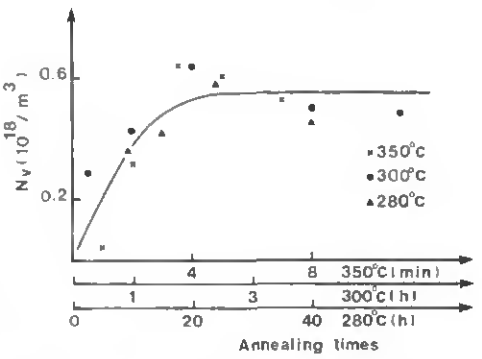

Fig. 12. The number of eutectic colonies formed on annealing alloy 2.

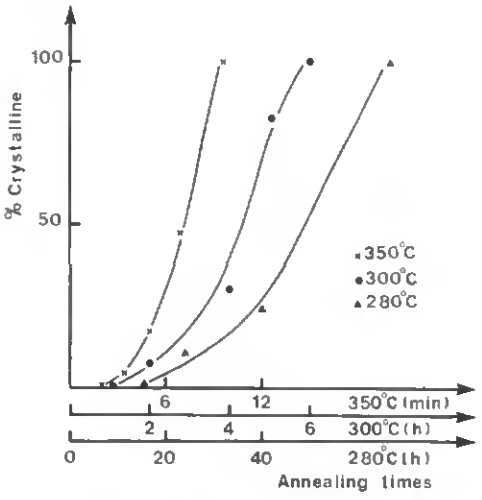

Fig. 14. Overall crystallization kinetics for alloy 2 at the three annealing temperatures.

inhomogeneities. The activation energy for nucleation is calculated to be about 240 kJ/mol.

3.2.3. Crystal growth. The crystal growth kinetics are given in Fig. 13. Once again the eutectic colonies had major/minor axes in a ratio of 2/1 to 3/1, maintained for each temperature and time. Growth occurs linearly in time to the completion of crystallization, with a temperature dependence described by an Arrhenius equation with activation energy of 230 kJ/mol.

3.2.4. Overall crystallization kinetics. The overall crystallization kinetics at each temperature are shown in Fig. 14 and reflect the slow initial rate of crystallization during the period of early nucleation.

3.3. Alloy 3 (nickel–3.8% titanium–18.2% boron)

3.3.1. General morphology. This alloy has a composition closer to that of the τ phase, and indeed crystallizes by the formation of facetted crystals of the τ phase alone, see Fig. 15. Even to the final stages of crystallization there was no evidence of second phase formation, indicating the difficulty of nucleating other phases and that the τ phase must have a non-equilibrium composition (equilibrium studies show a rather limited composition range for the τ phase in the Ni–Ti–B system [10]). Following the determination of a somewhat higher crystallization temperature of 412°C by scanning calorimetry (heating rate 40°C/min), crystallization studies were conducted at 300, 350 and 375°C.

3.3.2. Crystal nucleation. The number of crystals formed at each temperature is shown in Fig. 16. The nucleation of τ phase crystals continues at the same rate, for each temperature, over the entire period of crystallization. The number of crystals formed is extremely high, of the order of $300/\mu m^3$ or $3 \times 10^{20}/m^3$.

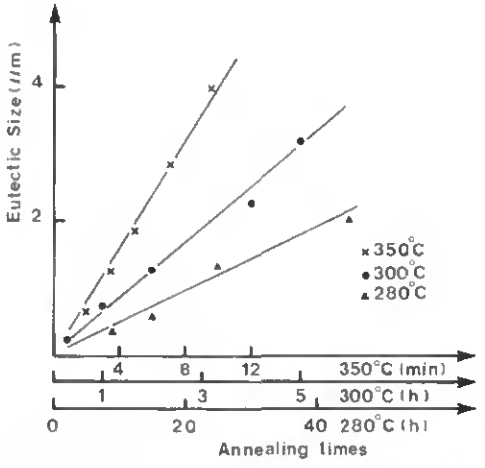

Fig. 13. Growth of the eutectic colonies on annealing alloy 2 at temperatures of 350, 300 and 280°C. The maximum size of the eutectic along its major axis is shown in each case.

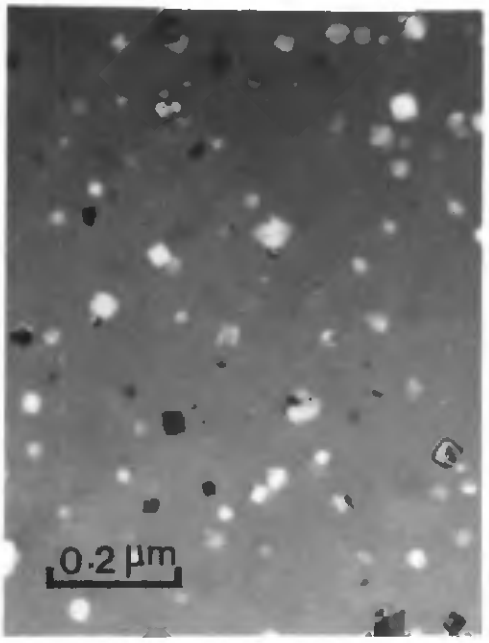

Fig. 15. Typical morphology of crystals formed on annealing alloy 3. Facetted crystals of the complex cubic boride phase only are seen.

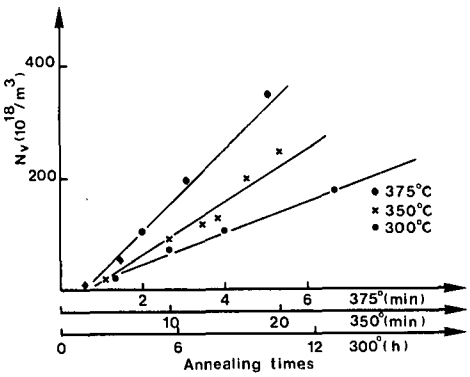

Fig. 16. The number of τ phase crystals formed on annealing alloy 3 at each temperature.

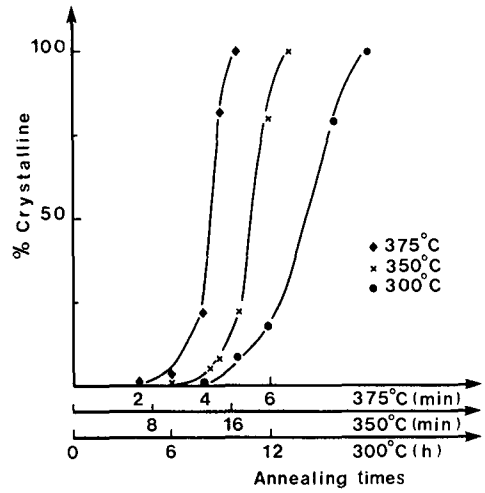

Fig. 18. Overall crystallization kinetics for alloy 3 at the three annealing temperatures.

These two observations, of constant nucleation rate throughout crystallization and of a very large number of crystals formed, both suggest that homogeneous nucleation may be occurring. The activation energy for nucleation was deduced to be 225 kJ/mol.

3.3.3. Crystal growth. The size of crystals formed on annealing is shown in Fig. 17. Crystal growth at each temperature occurs linearly in time to the completion of crystallization. The variation in growth rate with temperature corresponds to an activated process with an activation energy of 220 kJ/mol.

3.3.4. Overall crystallization kinetics. The overall crystallization kinetics at each temperature are shown in Fig. 18. The very slow start to crystallization is clearly seen. For this particular alloy the data were fitted to a Johnson–Mehl–Avrami equation to obtain a time exponent of 4 in accord with a transformation where both nucleation and growth rates remain constant throughout the transformation.

3.4. High resolution electron microscopy

High Resolution Electron Microscopy has been used specifically to examine the structure of crystal–glass interfaces for the various crystal structures found. It is at the same time possible to determine the structure of the crystalline phases present and thus confirm the previous diffraction analyses.

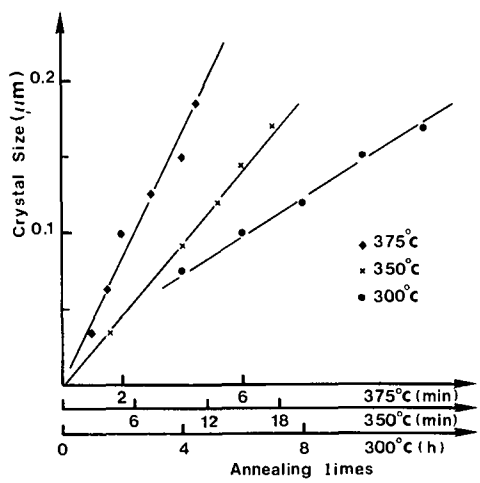

Fig. 17. Growth of τ phase crystals on annealing alloy 3 at 300, 350 and 375°C.

No serious attempt has been made to examine the structure of the glassy phase itself. Previous studies have sometimes detected microcrystalline-like regions within the glass [13] but otherwise have shown little more than random structures [14], particularly in view of the absence in these cases of atom columns through the foil thickness.

Figure 19 shows a τ phase particle within a sample of partially-crystallized alloy 1. The crystal has a reasonably well-defined square or diamond morphology. A number of defects traverses the crystal: these appear to be both twin and displacement faults which extend within the growing crystal. Attached to the τ phase crystal in an epitaxial manner, probably indicating the beginning of a eutectic colony formation, is a small crystal of γ nickel. This is shown in more detail in Fig. 20, as is a more detailed view of the τ phase–glass interface. A number of features of the interfaces should be noted: the τ phase-glass interface is facetted, showing a strong tendency for the {111} planes of the τ phase to lie along the interface; it is difficult to obtain good quality images of the ledges on these facetted interfaces which implies that these may not have strictly crystallographically-defined habit planes. In contrast, the γ nickel-glass interface, also illustrated in Fig. 20 does not appear to have such clearly-defined crystallographic facets and shows a more gently-curving interface. Note the epitaxial nucleation of the γnickel crystal on the τ phase with the {111} nickel planes parallel to the {111} τ phase planes: the {111} nickel planes and the {333} τ phase planes have almost precisely the same spacings.

Figure 21 shows a detailed view of the interface between a single orthorhombic boride needle and the glass. This orthorhombic needle is the typical

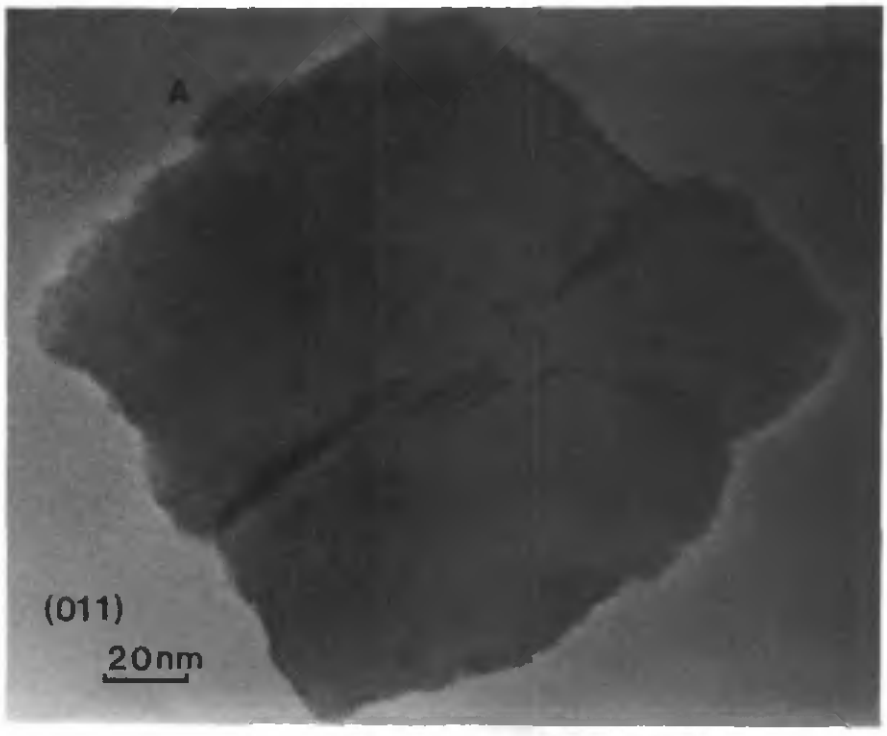

Fig. 19. High Resolution Electron Micrograph showing an isolated τ phase particle within partially-crystallized alloy 1. The crystal is oriented at the [011] orientation. Part of the crystal is rotated, in a twin relationship, and a stacking fault crosses the crystal. At A a small nickel crystal has formed epitaxially on the τ phase.

precursor of the large eutectic colonies observed. The needle axis is the [110] direction and the (110) and (001) planes are clearly visible within the needle. Most interestingly, the needle–glass interface is poorly defined and not obviously facetted. Clearly the absence of facetting implies a certain curvature of the interface within the thin foil, making the examination of interface structure even more difficult.

4. DISCUSSION

4.1. Summary of crystallization processes observed

Alloy 1, having close to the ternary–eutectic composition, crystallizes by the simultaneous formation of orthorhombic boride (O boride), complex cubic boride (τ phase) and face centre cubic nickel (γ phase). These three phases lead to three, independent primary crystallization processes). Primary O boride nucleates slowly and has a characteristic, high activation energy barrier. This phase is the only one to lead to the formation of fast-growing eutectic colonies as the γ nickel nucleates onto it. It is excessively time-consuming to distinguish between the τ phase and the γ nickel phase for quantitative analysis of the kinetics of nucleation and growth (no easy morphological distinction can be made) and these two phases are grouped together in the analysis of this alloy. These phases appear during the early stages of crystallization (hence we deduce a nucleation process occurs) and nucleation ceases, or at least slows, when still a small fraction of material has crystallized. We deduce that nucleation occurs on embryos which are present in fixed numbers in the quenched alloy. Exactly the same observation and analysis are made for the orthorhombic boride phase. For all three phases, the nucleation is deduced to occur on quenched-in embryos, present in fixed numbers, rather than by heterogeneous nucleation on impurities because the number of crystals formed is sometimes very high (up to $10^{20}/m^3$), and varies with the annealing temperature used and the phase considered; in addition there was no indication by electron microscopy of the presence of such impurity substrates.

The growth of the eutectic colonies as well as the single phase crystals occurs linearly with time for each annealing temperature used. It is a common observation [1, 3, 4] that the eutectic colonies grow at a constant rate because the chemical composition change between the eutectic and the glassy matrix is negligible or zero, and the diffusion distance required to separate the glassy alloy into the eutectic phases is small and constant. On the other hand the growth rate of primary, single-phase crystals is normally considered to be diffusion controlled [2, 4] and accordingly time dependent (crystal size proportional to $\sqrt{\text{time}}$). Several comments can be made concerning the growth of these small crystals:

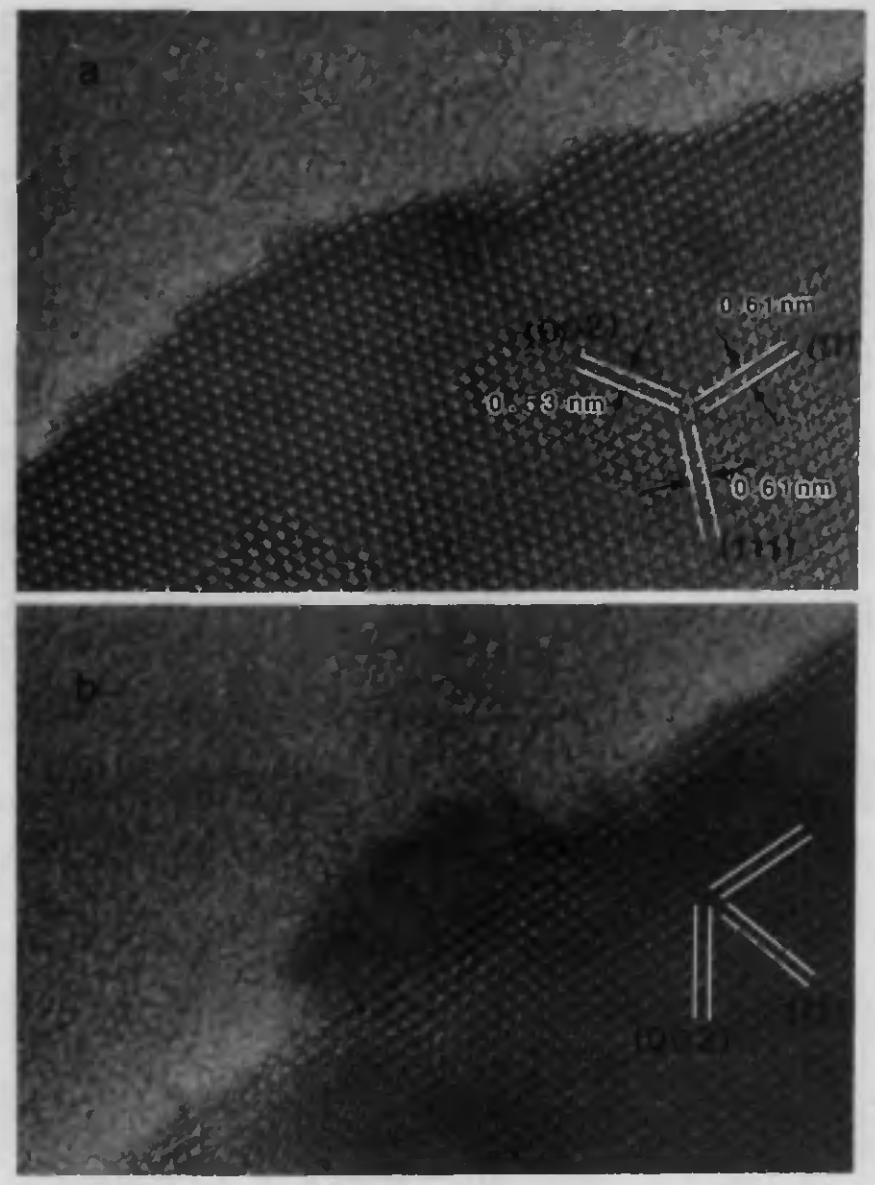

Fig. 20. Detailed views of the τ phase particle–glass interface (a) and the nickel particle (b) from Fig. 19.

—that growth is controlled by an interface process rather than a long-range diffusion process;
—the large number of particles formed means that diffusion fields of neighbouring particles quickly overlap.

It has been shown that the τ phase particles have well-facetted interfaces and accordingly their growth is probably interface-controlled and not diffusion-controlled. There is, however, no evidence to support the proposition of interface-transfer control of growtb of the γ nickel crystals. The large number of crystals present, even early during crystallization (for example, greater than 10 crystals per cubic micron), combined with the fairly large size of the crystals at these early stages (for example, 70–200 nm) means that the diffusion fields of adjacent particles rapidly overlap (for the cases given here the ratio of inter-particle spacing to particle size is only 3/1 to 6/1). Under such conditions the growth rate dependence will not be that of the simple square-root-time deduced under conditions of isolated particle growth [15]. It is difficult, however, to fully understand the observed constant growth rate may be produced by an unsteady, non-equilibrium growth mechanism.

Alloy 2, which has a composition only slightly different, but sufficiently closer towards the orthorhombic boride composition, crystallizes by the formation of the eutectic colonies of O boride and γ nickel with no sign of τ phase. The crystallization process is one of the rapid nucleation of the O boride, followed by the easy nucleation of the γ nickel on the boride-glass interface, and allowing the rapid,

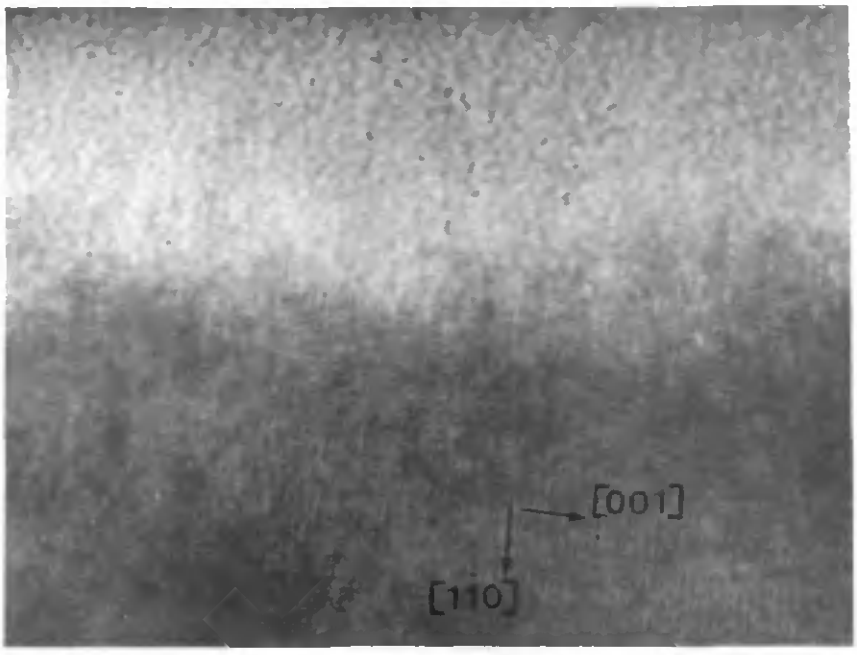

Fig. 21. High Resolution Electron Micrograph showing an isolated orthorhombic boride needle in partially-crystallized alloy 1. The needle axis is the [001]. The part of the interface shown is approximately parallel to the (110) plane, with the (001) planes perpendicular. Orthorhombic unit cell parameters: $a = 0.52$ nm; $b = 0.66$ nm; $c = 0.43$ nm. No evidence of facetting of the interfaces is seen.

time-independent growth of large eutectic colonies. Many more eutectic colonies form than for the case of alloy 1, and again the model of thermally-activated nucleation on quenched-in clusters applies.

Alloy 3 has a composition slightly closer to that of the complex-cubic τ phases and crystallizes by the formation of τ phase alone. The nucleation rate of τ phase remains constant throughout the entire crystallization process, as does the growth rate. The constancy of nucleation rate observed, for a given annealing temperature, together with the very high number of crystals which form (about $3 \times 10^{20}/m^3$) suggest that homogeneous nucleation occurs. The constant growth rate observed for each temperature follows from the facetted nature of the τ phase–glass interface and indicates that growth is controlled by interface-transfer kinetics.

4.2. Nucleation mechanisms during crystallization

The growth processes observed here have been relatively simple to examine and are interpreted in terms of eutectic growth, and single phase growth controlled by interface-transfer kinetics of by diffusion control under conditions where the diffusion fields significantly interact: in all cases linear growth with time is obtained.

For the present alloys, a more sensitive factor controlling crystallization is the nucleation process. This is important both in determining the speed at which crystallization occurs and the character of the phases to be obtained. For example, Fig. 22 shows that the fraction of eutectic phase obtained during the crystallization of the alloy 1 is highly sensitive to the annealing temperature chosen. The formation of the eutectic colony has been shown to take place in the sequence O boride→O boride + γ nickel (Fig. 7). The nucleation of the O boride is deduced to be controlled by a process having a relatively high activation energy (275 kJ/mol) and this leads to a strong variation in nucleation rate with temperature (Fig. 5). Accordingly, the choice of the annealing temperature allows the selection of crystal morphology and nature (Fig. 22): at high temperatures crystallization leads to the predominant appearance of the O boride + γ nickel eutectic; at low temperature crystallization leads almost entirely to the formation of single phase γ nickel and τ phase crystals.

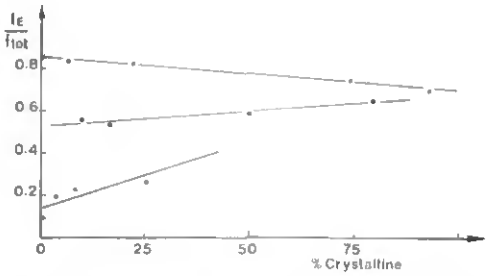

Fig. 22. The fraction of crystallized material present as eutectic phase mixture (O boride + γ nickel) as a function of the annealing temperature and time. At low temperatures, the difficulty of nucleating the eutectic structures means that predominantly a primary crystallization mode of single phase τ phase and γ nickel is obtained [▲ 260°C; ● 300°C; × 350°C].

Two aspects of nucleation need to be considered: (i) the appearance of single crystals of τ phase, γ nickel, or O boride from the glass; and (ii) the formation of eutectic phase mixture by the nucleation of a second phase onto the first.

(i) The relative rates of nucleation of τ phase, γ nickel and O boride will essentially be examined in terms of the homogeneous nucleation model. It could subsequently be supposed that a quenched-in embryo size distribution could explain the decay or saturation in nucleation rate observed here. According to the classical nucleation theory, the nucleation rate will most strongly be affected by the surface energy of the crystal-glass interface. Alternatively, it may be supposed that it is the number and type of the pre-existing, quenched-in short range ordered clusters which will determine the phase selection and kinetics of nucleation: for example, Walter and Berkowitz have analysed the formation of a tetragonal iron boride in terms of favourable Fe_3B clusters pre-existing in the as-quenched glass [7].

In alloy 1, which has a composition very close to that of the ternary eutectic composition, we can expect all three phases (O boride, γ nickel and τ phase) to have about the same likelihood of formation, at least under near-equilibrium conditions. However, the number of O boride crystals forming is very much less than the number of γ nickel and τ phase crystals, typically hundreds of times fewer crystals. As a basis for analysis we shall use the model developed by Spaepen [8, 9], namely that the crystal-glass interface energy can be considered to be determined by the entropy of the interface—hence by the entropy difference between the crystal and glass structure. Accordingly a more highly-ordered crystal structure (for example the O boride and τ phase) would lead to a larger entropy change at the interface and be associated with a higher energy. The High Resolution Electron Micrographs (Figs 19–21) give direct information on the structure of these crystal–glass interfaces and show that the interface structure is not as simply predicted as supposed above. The less ordered γ nickel structure (with a certain associated solubility of alloying elements) should have a relatively disordered interface with the glass, as observed in Fig. 20: nucleation is predicted to be relatively easy. The more highly-ordered τ phase (with restricted solubility of alloying elements) should have a more highly-ordered (facetted) interface, as observed in Figs 19 and 20: nucleation should be much slower than is in fact observed. The highly-ordered O boride (with, in addition, virtually no solubility of alloying elements) should have a highly-ordered interface: the interface between this boride and the glass appears to be very poorly ordered, Fig. 21, and yet nevertheless a very low nucleation rate is observed. Based on these observations it is deduced that the Spaepen model description of interface energy determined by the entropy of the crystal–glass interface [8, 9], in association with the homogeneous nucleation model assuming an equilibrium embryo distribution, is not capable of explaining the experimental results on nucleation rate differences.

Consequently, it would appear that it is the quenched-in, short-range-ordered clusters present within the glass which are responsible for the ease or difficulty of nucleation of a given crystal species. Within the alloy 1 the number of short range ordered clusters favourable to the nucleation of the O boride is very limited, leading to slow nucleation of this phase and a decay and halt in nucleation as the available clusters are exhausted. In this sense, the change of alloy composition towards that of the orthorhombic boride allows a much more favourable formation of clusters suitable for the nucleation of this phase: at the same time the number of clusters favourable to the formation of the γ nickel and τ phase decreases considerably. In an analogous way, alloy 3, with a composition slightly closer to that of the τ phase, will possess clusters eminently suitable for the formation of this phase but essentially none suitable for γ nickel or O boride formation.

(ii) The sequence of nucleation leading to the large eutectic colonies has been that of O boride nucleation followed by epitaxial nucleation of γ nickel at the boride–glass interface (Fig. 7). The epitaxial nucleation of γ nickel on the τ phase has also been observed (Figs 19 and 20), but this has occurred much more rarely, has not been followed by the rapid growth of a $\gamma + \tau$ eutectic colony, and has played a minimal role in crystallization. The sequence reported here is, in both cases, that of a simple crystal structure (f.c.c.) forming on a substrate of more complex structure (complex f.c.c. or orthorhombic). Such a sequence of simple phase nucleating on complex phase, and not vice versa, has been reported on several occasions previously (e.g. [16–18]). The reason for such a sequence is not clearly understood and seems to involve a balance between the energies of the substrate-glass and substrate-new crystal interfaces.

In the particular case of the nucleation of γ Nickel on a τ phase particle, Figs 19 and 20, it is seen that the crystal of simple structure nucleates epitaxially on the crystal of complex structure: the $\{111\}$ planes are parallel in each structure and the spacing of the $\{111\}$ plane in the τ phase is almost exactly three times that of the $\{111\}$ interplanar spacing in the γ nickel. It may be considered easier to assemble the simple unit cell (nickel) on the pre-existing, facetted τ phase substrate than to assemble a complex unit cell of τ phase on the pre-existing, non-facetted nickel substrate.

5. CONCLUSIONS

The study of the crystallization behaviour of three nickel–titanium–boron glassy alloys has examined in particular the influence of alloy composition and annealing temperature on the nucleation and growth processes occurring and related this to studies of

crystal–glass interfaces by High Resolution Electron Microscopy.

The nucleation of crystal phases occurs by a thermally-activated mechanism on a limited site-density such that nucleation often slows or stops during the early part of crystallization. The number of nuclei formed varies greatly from alloy to alloy and according to the crystal species considered.

The High Resolution Electron Microscope studies show that the crystal glass interfaces are not simply related to the complexity of the crystal structure: disordered interfaces are observed at the orthorhombic boride and Nickel phases which form in the glass; an ordered, facetted interface is observed at the complex cubic boride–glass interface. Based on the Spaepen model relating the crystal–glass interface energy to the entropy difference at the boundary, and assuming steady-state homogeneous nucleation on an equilibrium embryo distribution, it is not possible to explain the observed differences in nucleation rate. It is therefore concluded that it is the presence and number of suitable, quenched-in, short range ordered clusters that determine the kinetics and phases of nucleation.

Growth of the crystals formed may occur by a fast, eutectic mechanism or by single crystal growth. The single crystal growth may be controlled by an interface-transfer mechanism, observed here for the facetted crystals, or by long-range diffusion control.

The eutectic colonies are formed only by a sequence of complex phase nucleation, followed by simpler phase nucleation onto the first. This sequence, observed significantly here only for the orthorhombic boride and the Nickel phase, is followed by the very rapid growth of such colonies such that crystallization is dominated by such eutectic colony formation. The control of the two-stage nucleation sequence allows a sensitive control of crystallization kinetics and products.

Acknowledgements—We are grateful to Dr M. A. Morris for the many lively and stimulating discussions held during the course of this work and to Professor H.-J. Güntherodt for supplying the ribbons. The initial parts of the work were carried out in the laboratories of Professor J. L. Martin, EPF at Lausanne under the sponsorship of the Swiss Commission for the Encouragement of Scientific Research. The support of the Swiss National Science Foundation is gratefully acknowledged for support of the latter parts of the work. This work was carried out in partial fulfilment of doctoral requirements by one of us (N.M.).

REFERENCES

1. H. A. Davies, *Amorphous Metallic Alloys* (edited by F. E. Luborsky), Chap. 2, p. 8. Butterworths, London, (1983).
2. M. G. Scott, *ibid.* Chap. 10, p. 144.
3. K. Muller and M. Von Heimendahl, *J. Mater. Sci.* **17,** 2525 (1982).
4. U. Koster and U. Herold, *Glassy Metals* (edited by H.-J. Güntherodt and H. Beck). Springer, Berlin (1981).
5. H. A. Davies, *Phys. Chem. Glasses* **17,** 159 (1976).
6. D. G. Morris, *Acta metall.* **29,** 1213 (1981).
7. J.- L. Walter and A. E. Berkowitz, *J. Mater. Sci.* **20,** 1471 (1985).
8. F. Spaepen, *Acta metall.* **23,** 729 (1975).
9. F. Spaepen and R. B. Meyer, *Scripta metall.* **10,** 257 (1976).
10. J. D. Schobel and H. H. Stadelmaier, *Metall.* **19,** 715 (1965).
11. R. S. Tiwari, S. Ranganathan and M. v. Heimendahl, *Z. Metallk.* **72,** 563 (1981).
12. L. W. Cahn and J. Nutting, *Trans. metall. Soc. A.I.M.E.* **215,** 526 (1959).
13. P. H. Gaskell, L. A. Freeman and D. J. Smith, *Proc. 4th Int. Conf. on Rapidly Quenched Metals*, Sendai (edited by T. Masumoto and K. Suzuki), p. 439. Japan Inst. Metals (1982).
14. H. Ino, H. Ichinose and K. Nagata, *Proc. 5th Int. Conf. on Rapidly Quenched Metals*, Wurtzburg (edited by S. Steeb and H. Warlimont), p. 263. Elsevier, Amsterdam (1985).
15. J. W. Martin and R. D. Doherty, *Stability of Microstructure in Metallic Systems.* Cambridge Univ. Press (1976).
16. R. S. Tiwari and M. v. Heimendahl, *Scripta metall.* **15,** 809 (1981).
17. B. E. Sundquist and L. F. Mondolfo, *Trans. metall. Soc. A.I.M.E.* **221,** 157 (1961).
18. P. B. Crosley, A. W. Douglas and L. F. Mondolfo, *The Solidification of Metals*, Vol, 110, p. 74. ISI Publication (1968).

Submitted . J. Mat. Sci.

Ductilisation and Embrittlement during the crystallization of Ni-Ti-B glasses

N. Merk, D.G. Morris and M.A. Morris, Institute of Structural Metallurgy, University of Neuchâtel, 2000 Neuchâtel (Switzerland)

Abstract

The fracture responses of three Ni-Ti-B glasses have been studied during the very early stages of crystallization. Comparison of alloys leads to a separation of relaxation and crystallization effects. The tendency toward reductilisation in the presence of a small quantity of crystalline particles is directly related to the fine distribution and very small size of these particles which tend to interrupt concentrated shear without causing significant localised failure. Such particles thereby tend to distribute homogeneously the plastic deformation and to compensate the simultaneous relaxation embrittlement.

Introduction

Relaxation and crystallization embrittlement have previously been reported in a wide range of transition metal-metalloïd glasses [1,2]. The relaxation phenomenon has been attributed to the loss of free volume leading to a difficulty of plastic deformation. The embrittlement intensity and flow behaviour depend on the atomic and electronic nature of the elements [3]. A tendency to phase separation or clustering during relaxation has also been evoked as a cause of embrittlement [4]. In $Fe_{40}Ni_{40}B_{20}$ glass, the formation of an extremely fine dispersion of $(Fe,Ni)_3B$ particles has been found to embrittle the glass when their size exceeds 2.5-3 nm [5]. Auger analysis of $Fe_{40}Ni_{40}P_{14}B_6$ [6] indicates that during annealing segregation occurs into

discrete regions of less than 6 nm in size. These regions of high P concentration cause embrittlement and are nuclei for crystals less ductile than the matrix. Thus subsequent crystallization embrittlement would be expected.

Such a loss of ductility is normally catastrophic and can prevent practical applications of metallic glasses. Obtaining alloys for which the ductility remains high even after introducing crystalline phases (formed during crystallization or due to a low cooling rate) would be desirable. In very rare cases, a partial reductilisation of the material at the onset of crystallization has been reported, for example $Fe_{41}Ni_{41}B_{18}$ is reductilised when primary crystals of γ(Fe,Ni) appear [7]. If aging continues, a brittle Fe_3B phase appears which leads to the reappearance of embrittlement. The partial ductilisation of Fe-B alloys during crystallization has been attributed to the presence of a few small, soft particles [8]. The creation of these soft particles within the glass liberates new free volume and hence the glass reacquires a facility for plastic deformation. The subsequent embrittlement which occurs when aging continues has been explained by the enrichment of the matrix in boron which tends to trap the free volume and hence to embrittle the material. Depending on their composition, Fe-Ni-Zr alloys containing Nb or Ta [9] tend to be more or less ductile even for a significant fraction of crystallization and in the presence of hard particles. $Fe_{40}Ni_{20}Zr_9Nb$ has the best ductility during crystallization of all the alloys studied, remaining ductile up to 30 % crystallization, and in particular has the smallest crystal average size (compared to the other alloys). This observation suggests a certain relationship between the size of the particle present and the overall ductility of the material.

This paper describes the changes in fracture behaviour observed during the crystallization of a series of Ni-Ti-B glasses. These glasses form different phases during crystallization and thus it is possible to relate the mechanical response to the phase nature as well as to the distribution of these crystalline particles. In this paper we analyse the reductilisation effect of small amounts of crystallinity, and in a second paper we develop a model for the crystallization embrittlement which follows.

Experimental details

Three alloys of composition: $Ni\text{-}B_{19.1}Ti_{2.1}$ (alloy A), $Ni\text{-}B_{18.2}Ti_{3.8}$ (alloy B) and $Ni\text{-}B_{17.9}\ Ti_3$ (alloy C) have been melt spun (courtesy of Professor Güntherodt, University of Basel) as ribbons ~ 9 mm wide and ~ 20 μm thick. Microstructural studies were carried out using a variety of annealing conditions in parallel with toughness tests and fracture surface examinations. Heat treatments were performed in a salt bath or in a furnace under argon atmosphere. The microstructures were characterized (crystal nature, size and distribution) using a Hitachi H-700 TEM operating at 200 kV. Fracture toughness tests were performed in an Instron testing machine on polished specimens with a 2 mm long centre notch introduced by spark erosion (before heat treatment) using a 100 μm thick copper-foil electrode. The 2.5 cm long samples were glued to plate grips and pulled at a constant displacement rate of 0.2 mm/min. The localised deformation at the notch was independent of sample irregularities (or grip stress-concentrations) leading to highly reproducible (± 15 %) data. For each condition 4 to 6 samples were tested, obviously imperfect samples were discounted, and finally the fracture toughness estimated to within ± 5 to

10 %. Fracture toughness was calculated from the failure load using standard stress-intensity formulae. The resulting fracture surfaces have been observed and characterised using a Cambridge 250 Scanning Electron Microscope.

Results

A typical microstructure of each partially crystallized alloy is shown in figure 1. Alloy A (fig. 1a) crystallises following a eutectic process leading to the formation of a mixture of orthorhombic Ni_3B and fcc Nickel. Alloy B (fig. 1b) contains primary crystals of τ phase ($M_{23}B_6$). Alloy C (fig. 1c) crystallises by the simultaneous formation of three phases - the lamellar, cigar-shaped eutectic colonies (as in alloy A) together with the small facetted τ phase crystals (as in alloy B) and small irregular-shaped crystals of fcc Nickel. Details of the crystallization kinetics have been reported previously [10].

The results of the toughness tests following heat treatment at 300 °C are presented in figure 2. For each alloy a similar evolution of the fracture toughness has been obtained as crystallization takes place at different annealing temperatures. At the fully crystalline state all three alloys have lost as much as 3/4 of the original toughness. The evolution of toughness for each alloy is not identical, however. While alloy A (fig. 2a) undergoes a sharp and continuous decrease in toughness, alloy C (fig. 2c) shows a small initial increase in toughness [this increase is much more prominant at the highest annealing temperature (350 °C, see also fig. 7) and not observed at the lowest temperature] and alloy B (fig. 2b) shows essentially two stages of embrittlement with a short toughness plateau between the two stages. The toughness value at the plateau for alloy B

increases with temperature, 25 $MN/m^3/_2$ at 300 °C, 27 $MN/m^3/_2$ at 350 °C and 34 $MN/m^3/_2$ at 375 °C. As shown in fig. 2b, annealing for only 15 minutes leads already to a toughness reduction of 2 $MN/m^3/_2$. Since the fraction of crystalline material does not exceed 10^{-6} during the first hour of heat treatment, the observed embrittlement can be attributed totally to the relaxation effect.

For alloy B, annealing from 2 to 6 hours leads to an increase in the fraction of crystalline material from 10^{-5} to 7.10^{-3}. During this period the average crystal size (10 nm at 2 h) increases to 30 nm. Two possible explanations can be proposed to explain the fracture behaviour during this early crystallization stage of the alloy. One explanation is that the relaxation embrittlement reaches an end before crystallization embrittlement starts and the other possibility is that the continuing relaxation embrittlement is temporarily balanced by a ductilisation tendency due to the presence of the very first crystals, with crystallization embrittlement taking place subsequently. As will be shown later, this second possibility seems more likely.

In our alloys, both in the glassy state as well as the partially crystalline state, fracture occurs by a shear mechanism on a well-defined macroscopic shear plane oriented at 45 ° to the tensile axis. Initially, the fracture surfaces of all three alloys contain the two typical zones of fractured glassy metals: the shear offset which is a smooth zone formed during initial shearing and the veined zone formed during final fracture. In order to demonstrate the morphology change during crystallization, a sequence of fracture surfaces of alloy A and B is presented in figure 3. As crystallization takes place, several changes occur. In particular it may be

noted that the vein pattern has changed into a dimple structure, reflecting the influence of the internal microstructures (figs. 1a and 1b). Nevertheless in both cases as more and more crystallization occurs, the offset decreases and the density of dimples increases. In this sense, the offset (Δ) and the average dimple size (D) can be chosen as parameters characterizing the fracture surfaces and the changes occurring. The decreases in offset and dimple size during annealing of alloys A and B at three different temperatures are presented in figure 4. For alloy A, the offset and the dimple size decrease at very much the same rates for a given temperature and, furthermore, there is a clear correspondance between D an Δ for each fracture surface condition (see fig. 3I). In comparison, for alloy B, the dimple size decreases at a much faster rate than the offset (see fig. 3II). For alloy C, the fracture surface parameters (Δ and D) decrease during crystallization in much the same way as alloy B.

The importance of the fracture surface morphology in relation to the toughness is indicated by figure 5 where a clear relationship between the toughness and the square root of the offset is seen for all three alloys. The values of the slopes of the lines obtained are 16 GN/m^2 for alloy A, 10-22 GN/m^2 for alloy B and 20 GN/m^2 for alloy C.

Discussion

Independent of the alloy composition, a loss of ductility seems unavoidable during annealing. Both relaxation and crystallization have an embrittlement effect on glasses. Nevertheless, as illustrated in fig. 2c, at the very early stages of crystallization a slight ductilisation may be achieved in

some cases. For example, during the first hour at 300 °C, the alloy C shows a slight increase in ductility. During this period, the fracture of crystalline material reaches 10^{-4} with an average size of the small particles (τ and fccNi) of 35 nm (after 1 h) and an average size of eutectic colonies of 250 nm (after 1 h).

Since alloy B shows only relaxation embrittlement during the first hours of heat treatment (at 300 °C) a comparison of alloys B and C will allow a separation of the different effects. In order to make this separation we shall assume that the relaxation effect and the kinetics of relaxation are similar for the two alloys. Considering the very slight difference in composition between the alloys and the fact that the ribbons have been made at essentially the same cooling rate, under the same casting conditions, the glass transition temperature T_g of the alloys should be very close to each other. This assumption has been confirmed in several previous studies in which a small change in composition has been shown to lead to only a small change in T_g [11,12,13]. In addition, it has been reported on several occasions that the relaxation kinetics in a given transition metal-metalloïd system are similar for alloys containing between 16.5 to 28.9 atomic percent of metalloïd [14,15] (around an eutectic composition).

Thus, with the assumption of the same relaxation kinetics during annealing (for each temperature) for the two alloys B and C, the superposition of the fracture toughnesses allows the various factors affecting toughness to be separated. Figures 6 and 7 show the superposition of the two toughness curves (alloys Band C) at 300 °C and 350 °C. In the period of 0 to 1 hour, at 300 °C, alloy B undergoes relaxation embrittlement only while during

this period alloy C already contains crystals of a certain size which compensate the matrix relaxation embrittlement. Thus the difference between the toughnesses of the two alloys (reported in figure 6c and 7c) from the initial value up to the first intersection of the two curves determines the region of crystallization ductilisation of alloy C. Since the initial toughness values are not equal, an upper and lower limit of the ductilisation domain can be defined by direct superposition of the experimental toughness data (figs. 6a and 7a) or by displacing the toughness data to an identical initial value for the two glasses (figs. 6b and 7b).

The same analysis performed on the 350 °C data (fig. 7) provides another example of this behaviour. In the period of 0 to 6 min, corresponding to the relaxation embrittlement of alloy B, the fraction of crystalline material in alloy C reaches 2.10^{-2}. After 6 min, the eutectic and small crystals are respectively of size 600 nm and 60 nm. It is over this period that ductilisation of alloy C is observed.

In a similar fashion, for the period of time during which alloy B shows a tendency toward ductilisation, the difference in toughness of alloys B and C determines the ductilisation domain of this alloy. An examination of the microstructures of alloy B over these stages confirms that the reductilisation tendency coincides with the first appearance of crystalline particles.

In table 1 the microstructural parameters corresponding to the condition of maximum ductilisation are summarized. The only common parameter between all conditions of ductilisation is the size of the small crystalline particles, namely about 25-35 nm, while the amount of crystallinity may vary from about 10^{-5} to near 10^{-2}: the eutectic particles do not appear to play a dominant role in determining the ductilisation effect.

In comparison with other glassy alloys in which crystallization ductilisation has been observed, it seems reasonable to associate ductilisation with a very small size of the crystalline particles. For example partially crystallized Fe-Ni-Zr alloys are ductile [9] before the average crystal size reaches 50 nm, independent of the crystal density. The crystals formed in this particular case, just as the present τ and orthorhombic Ni_3B particles, can be considered as rather hard particles, in contrast to the soft particles studied by Hillenbrand et al [7,8]. Rather it seems that crystal size instead of crystal nature, is the dominant factor determining ductilisation. According to this, the observed ductilisation in Fe-B glasses [7,8] can be interpreted in terms of particle size rather than particle nature (hard or soft). For this alloy, the loss of ductility takes place when the Fe_3B particles have nucleated and the particle average size has then reached about 150 nm [8].

Taking the size criterion as important for significant ductilisation, the reason why a ductilisation effect was not detected during crystallization of alloy A (and also for alloy C at 260 °C) is found. The first heat treatments used here produce already large particles corresponding to the

end of the ductilisation domain when crystallization embrittlement is already significant (bearing in mind that the crystallization process of alloy A is of eutectic type with a relatively fast crystal growth rate).

The ductilisation effect is observed in association with two embrittlement effects. One of these, relaxation embrittlement, has been explained in terms of free volume loss. In contrast the tendency towards ductilisation may then be related to the recreation of new free volume at the particle-matrix interface in view of the greater density of the crystal over that of the glass. This hypothesis assumes that the kinetics of relaxation are slower than those of crystallization, and hence that the free volume released remains, usefully, inside the glass. In our view it seems that ductilisation is more likely explained by the small particles acting as obstacles to intense planar shear, exactly as for particle dispersions within a crystalline material which distribute and homgenise shear.

In a similar way, crystallization embrittlement has been explained in terms of the reduction in strain necessary for cavity formation and growth [16]. It follows that for crystallization ductilisation to be observed stable cavities should not be easily formed at the particle-matrix interface. The dependence of particle size on stable cavity formation may be treated in terms of creating a critical stress concentration at the interface [17], and hence in terms of minimum necessary particle size. In addition, it may be that particles smaller than the shear band thickness (~ 20 nm [18]) may not yet be effective obstacles. Hence it is reasonable to suppose that for particles up to 25-30 nm in size (the condition of maximum ductilisation

shown in table I) the probability of stable cavity formation is low. Thus, the addition of the two effects (slip band obstruction without yet the possibility of easy nucleation) determines the range of crystallization ductilisation.

It is clear that growing particles, acting as stress raisers, will become more and more strong barriers against flow and hence more susceptible to cavity nucleation. The rate of cavity nucleation will increase with particle size and will eventually lead to the third domain of crystallization embrittlement.

Crystallization embrittlement is represented by the final fall in toughness (see fig. 2) towards the values charasteristic of the fully-crystalline states. Fracture occurs when the shear displacement reaches a critical value, the offset Δ measured on the fracture surfaces. The absence of work-hardening in the glass (as well as in the partially-crystallized glasses) allows us to relate the work done during shear fracture (G), the shear stress (τ_c) and the shear displacement (Δ).

At failure: $G_c = \tau_c \cdot \Delta$ (1)

(assuming that all the work is introduced as plastic deformation without work hardening at the fracture surface). According to Irwin [19] the fracture toughness can be related to the strain energy release rate, as:

$$K_{IC} = (EG)^{1/2}$$

by analogy, for the shear failure examined here, we can write

$$K_{IIIC} = (\mu G_C)^{1/2} \qquad (2)$$

where μ is the shear modulus, thus:

$$K_{IIIC} = (\mu \tau_C)^{1/2} \Delta^{1/2} \qquad (3)$$

which corresponds to the relation observed in fig. 5. Since the fracture toughness measured was based on the applied, longitudinal stress, the measured slope can best be related to about $(2\ \mu\tau_C)^1/_2$. It is clear that this value is not a constant during crystallization (the shear modulus can increase by up to 30 % during crystallization and also microhardness measurements performed on the present alloys show an increase of nearly 40 % during crystallization). Nevertheless as can be seen in fig. 5, the approximation of a constant slope is not unreasonable. Using literature values for the material parameters, μ = 50 GN/m^2 and $\tau_C = \sigma_y/2$ = 1.15 GN/m^2 [20] of Ni-based glasses, the slope $(2\mu\tau_C)^1/_2$ is deduced to be 12 GN/m^2 in reasonable agreement with the measured slopes from fig. 5 (10-20 GN/m^2). Some of the difference between the experimental and the calculated slopes may arise in the work required for final fracture, namely the ductile parting of the regions between the cavities.

From the above discussion, and particularly in view of the virtual constancy of τ_c for a given alloy, it is clear that the critical shear displacement Δ takes on an especially significant meaning as a parameter characterising failure. It has been shown that the values of Δ and D, the size of the dimples on the fracture surfaces, are closely related and also dependent on the types of particles present. This relationship, as well as an explicit model of the failure of semi-crystalline metallic alloys, will be treated in a later publication.

Conclusions

Different factors affecting the fracture behaviour during crystallization of three Ni-Ti-B glasses have been separated. A very first period of heat treatment corresponds to relaxation embrittlement and is followed and combined with a certain period of partial ductilisation at the onset of crystallization. Such ductilisation takes place when small particles (20-40 nm) are present which tend to inhibit the localised shear deformation characterising the glass and thereby to homogenise shear. The ductilisation effect is lost when the particles exceed a critical size for which cavitation at the particles becomes possible. The shear displacement necessary to cause such cavitation and then failure is representative of the toughness of the material.

References

[1] Luborsky, F.E. and Walter, J.L., J.Appl.Phys., 47, 3638 (1976).

[2] Kimura, H. and Ast, D.G., Proc. 4th Int. Conf. on Rapidly Quenched Metals, Eds. Masumoto, T. and Suzuki, K., Vol. I, p 457.

[3] Chen, H.S., Krause, J.T. and Coleman, E., J.Non Crystall.Solids, 8,(1975) 157; Scripta Met., 9 (1975) 787.

[4] Chen, H.S., Mat.Sci.Eng. 26 (1976) 79

[5] Piller, J. and Haasen, P., Acta Met. 30, (1982) 1.

[6] Walter, J.L., Bacon, F. and Luborsky, F.E., Mat.Sci.Eng. 24 (1976) 239.

[7] Jost, N., Hillenbrand, H.G. and Hornbogen, E., Proc. 5th Int.Conf. on Rapidly Quenched Metals, Eds. Warlimont H. and Steeb, S. (1985) Vol II, 1417.

[8] Hillenbrand, H.G., Hornbogen, E. and Köster, U., Proc. 4th Int. Conf. on Rapidly Quenched Metals, Eds. Masumoto, T. and Suzuki, K. (1982) Vol II, 1369.

[9] Inoue, A., Tomioka, H. and Masumoto, T., J. Mat.Sci 18 (1983) 153.

[10] Merk, N., Morris, D.G. and Stadelmann, P., Acta Met, in press.

[11] Naka, M., Nishi, Y. and Masumoto, T. Proc. 3th Int. Conf. on Rapidly Quenched Metals, Ed. Cantor B. The Metals Society, London (1978), Vol. I, 231.

[12] Reeve, J., Gregan, G.P., Davies, H.A., Proc. 5th Int. Conf. on Rapidly Quenched Metals, Eds. Warlimont, H. and Steeb, S. (1985), Vol. I, 203.

[13] Zielinski, P.G., Ostatek, J., Kizek, M. and Matyja, H., Proc. 3rd Int. Conf. on Rapidly Quenched Metals, Ed. Cantor, B. The Metals Society, London (1978), Vol. I, 337.

[14] Warlimont, H. and Gordelik, P., as ref. [12], Vol. I, 619.

[15] Gordelik, P. and Sommer, F., as ref. [12], Vol. I, 623.

[16] Freed, R.L. and Van der Sande, J.B., Acta Met 28 (1980), 103.

[17] Smith, E., Acta Met 14 (1966) 991.

[18] Masumoto, T. and Maddin, R., Acta Met 19 (1971) 725.

[19] Irwin, G.R., Applied Materials Research (1964) 3, 65.

[20] Davis, L.A., Metallic Glasses, ASM, Metals Park, Ohio (1978), 191.

Figure captions

figure 1: Typical microstructure of partially crystallized alloys: a) alloy A after 24 h at 280 °C; b) alloy B after 8 h at 300 °C and c) alloy C after 8 h at 300 °C.

figure 2: Toughness evolution during heat treatment at 300 °C for a) alloy A; b) alloy B and c) alloy C.

figure 3: Fracture surface evolution during crystallization of I) alloy A after 2,5 and 7 mins at 350 °C and II) alloy B after 4, 10 and 17 min at 350 °C.

figure 4: Variation of dimple size and offset with annealing time at three different annealing temperatures for a) alloy A and b) alloy B.

figure 5: Respresentation of toughness values as a function of the square root of offset for a) alloy A; b) alloy B and c) alloy C.

figure 6: Superposition of toughness curves at 300 °C for alloys Band C: a) using the measured toughness values; b) based on identical starting toughnesses for the two glasses; c) the difference of toughness for the two alloys allowing the determination of the ductilisation domain for each alloy. The two lines (continuous and dashed) indicate the range of ductilisation according to the toughness values used for comparison. The shaded area shows the ductilisation regime for alloy B and the open area that for alloy C.

figure 7: Superposition of toughness curves at 350 °C for alloys B and C: details are same as for fig. 6.

Table 1 Microstructural conditions corresponding to the maximum extent of ductilisation of alloys B and C.

		Annealing Temperature 260 °C	300 °C	350 °C	375 °C
Alloy C	Fraction crystalline	$<10^{-4}$	10^{-5}	10^{-4}	-
	Size of Eutectics	<100 nm	120 nm	150 nm	-
	Size of τ/γ crystals	<40 nm	25 nm	30 nm	-
	Distance between Eutectics	> 2 µm	6 µm	3 µm	-
	Dist. between small crystals	>0.8 µm	1.2 µm	0.6 µm	-
Alloy B	Fraction crystalline	-	10^{-3}	5.10^{-3}	$10^{-2},^{-3}$*
	Size of τ crystals	-	25 nm	30 nm	20-40 nm*
	Distance between crystals	-	0.5 µm	0.4 µm	0.3 µm*

* Values corresponding to the change in slope of toughness at the plateau observed during crystallization.

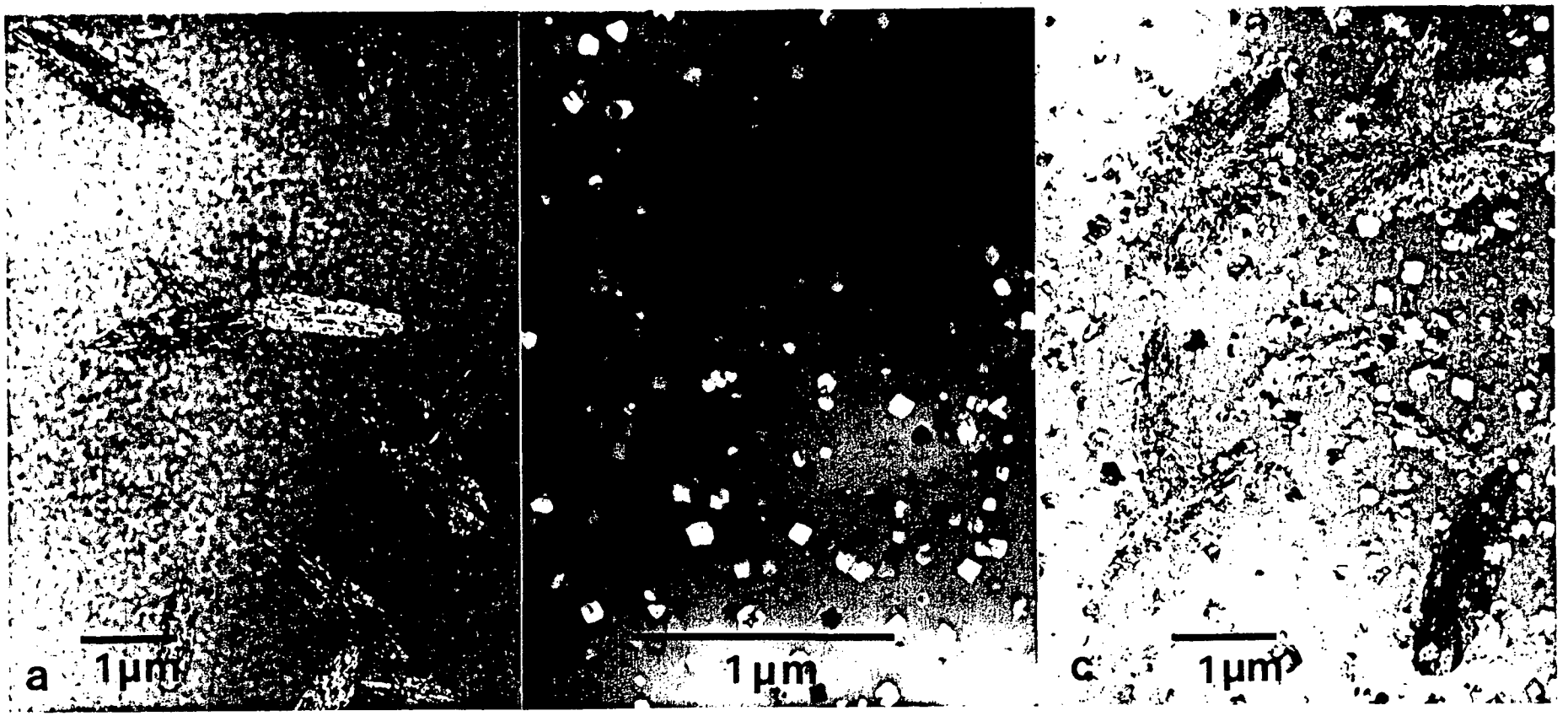

Fig 1 Mech-Morris-Morris

Fig 2a Merk/Morse/Morris

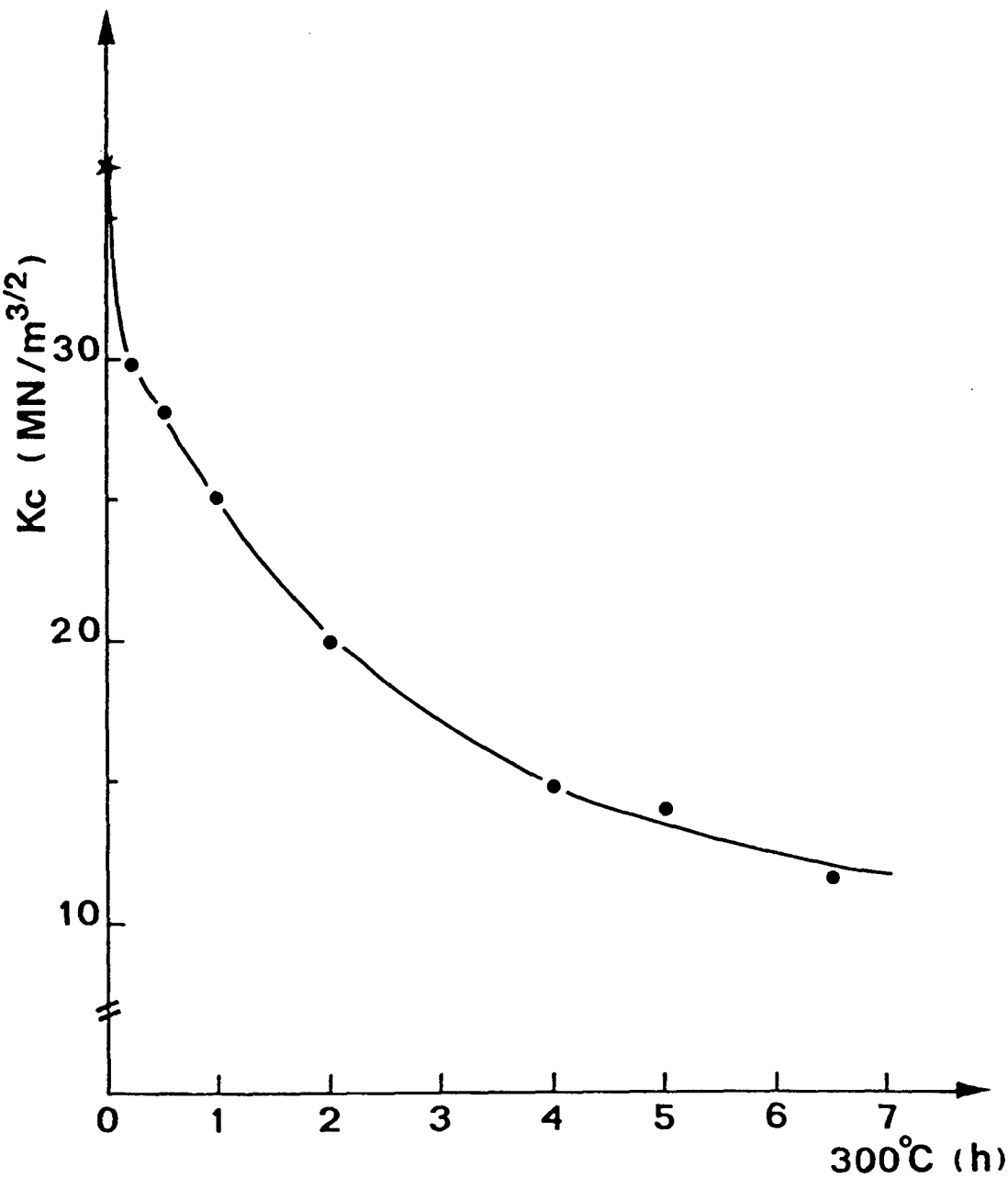

Fig 2 b Meh / Morn / Moni

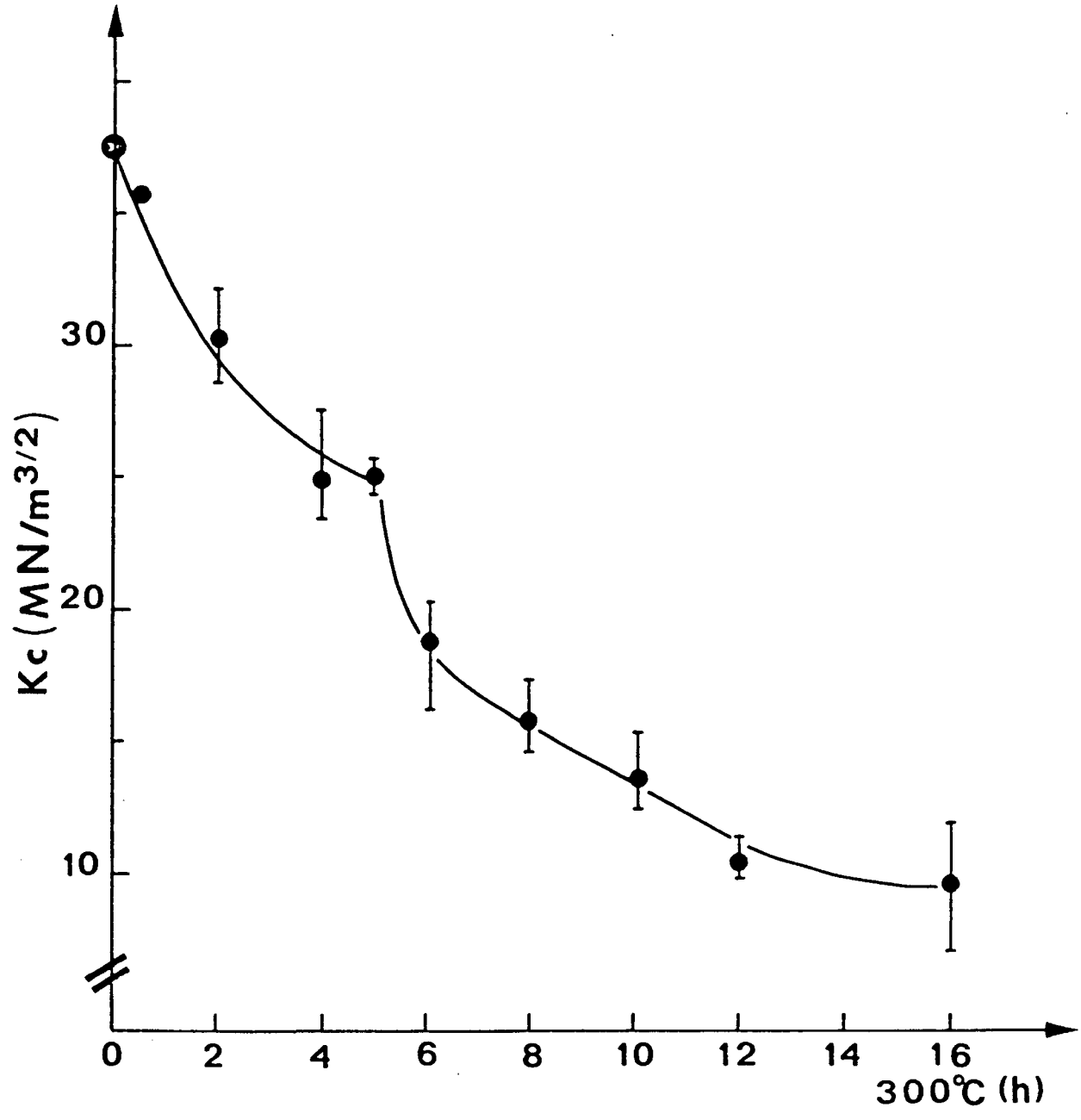

Fig 2c

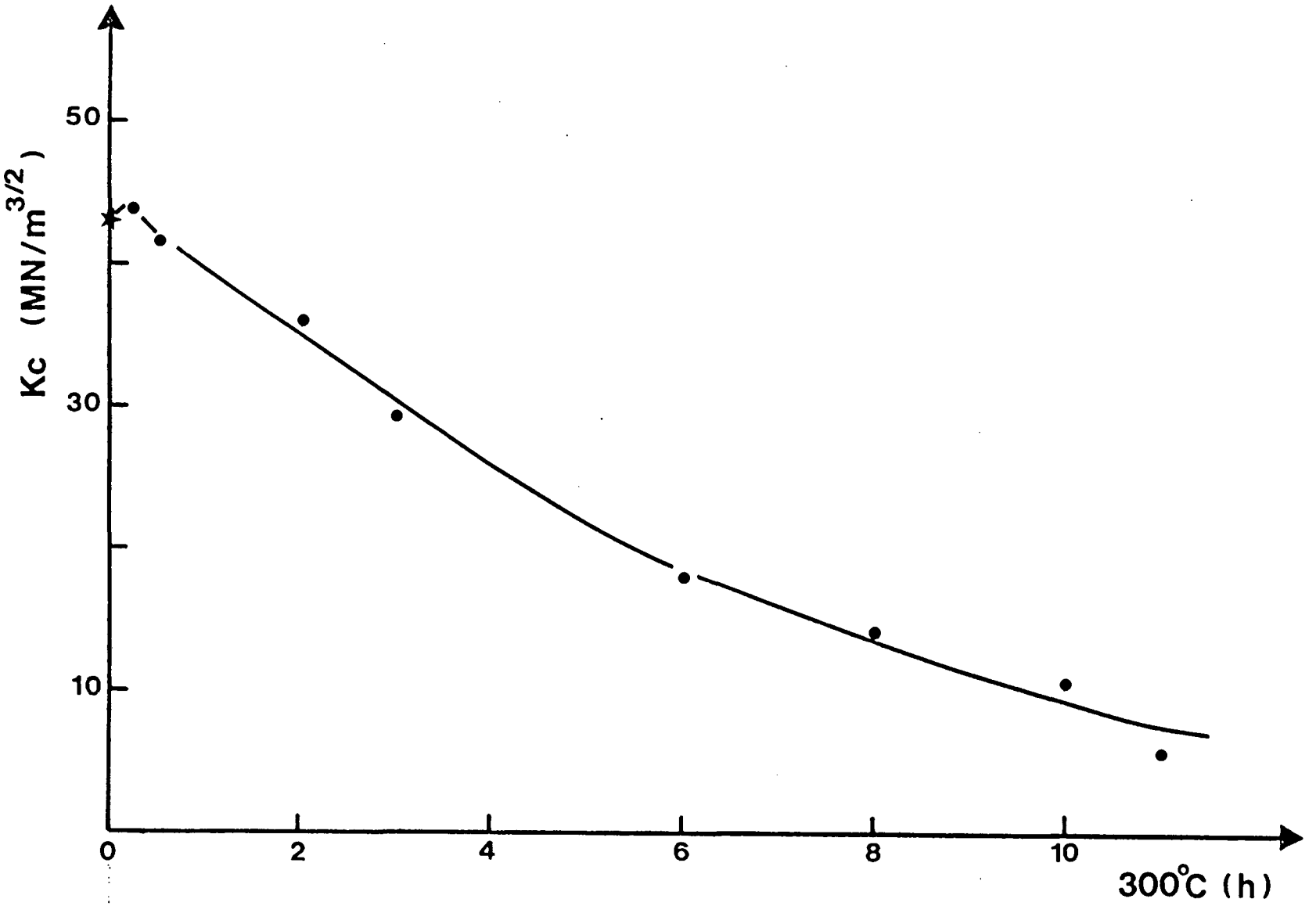

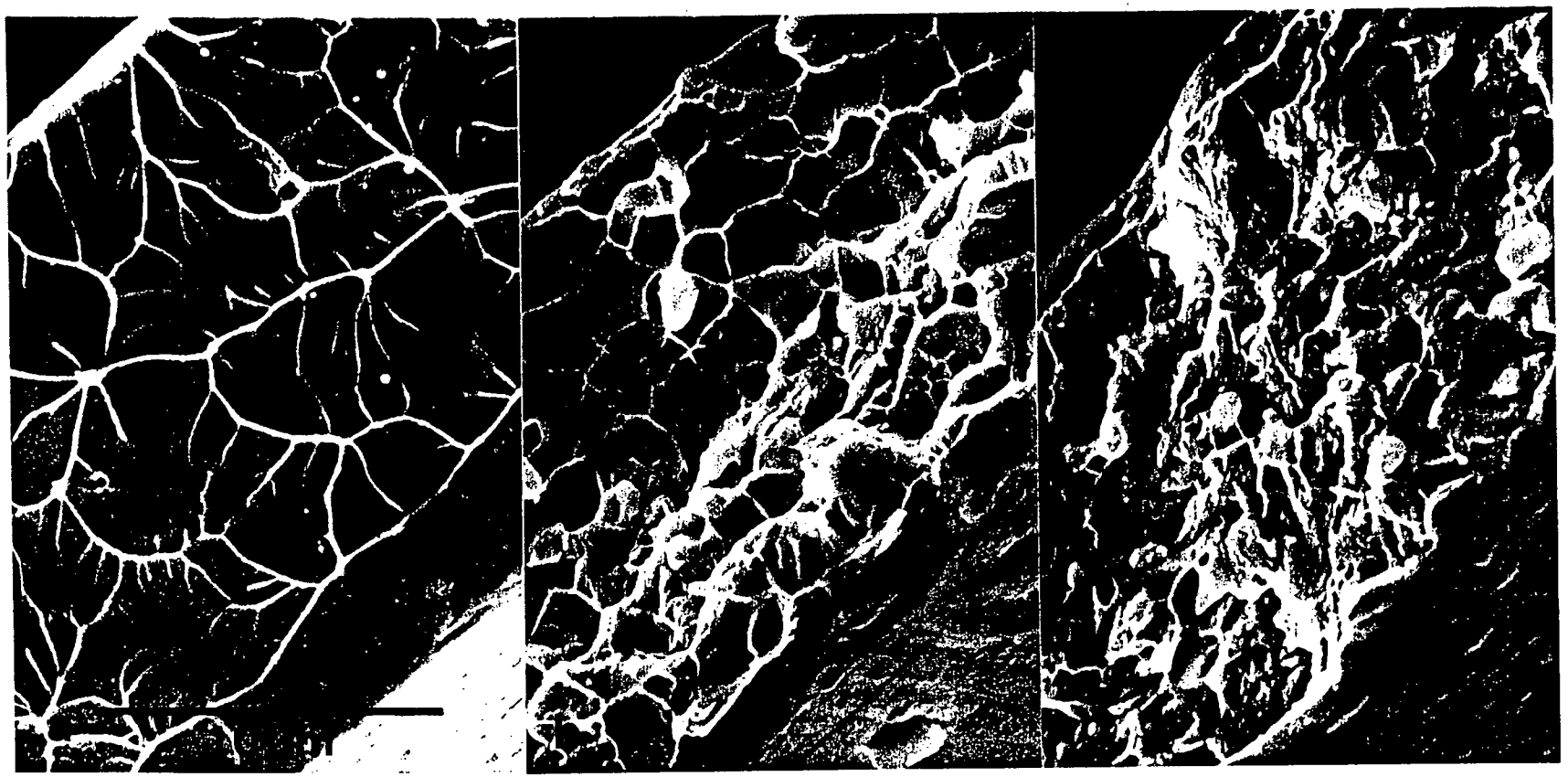

Fig 3 I Merle-Mono-Mono

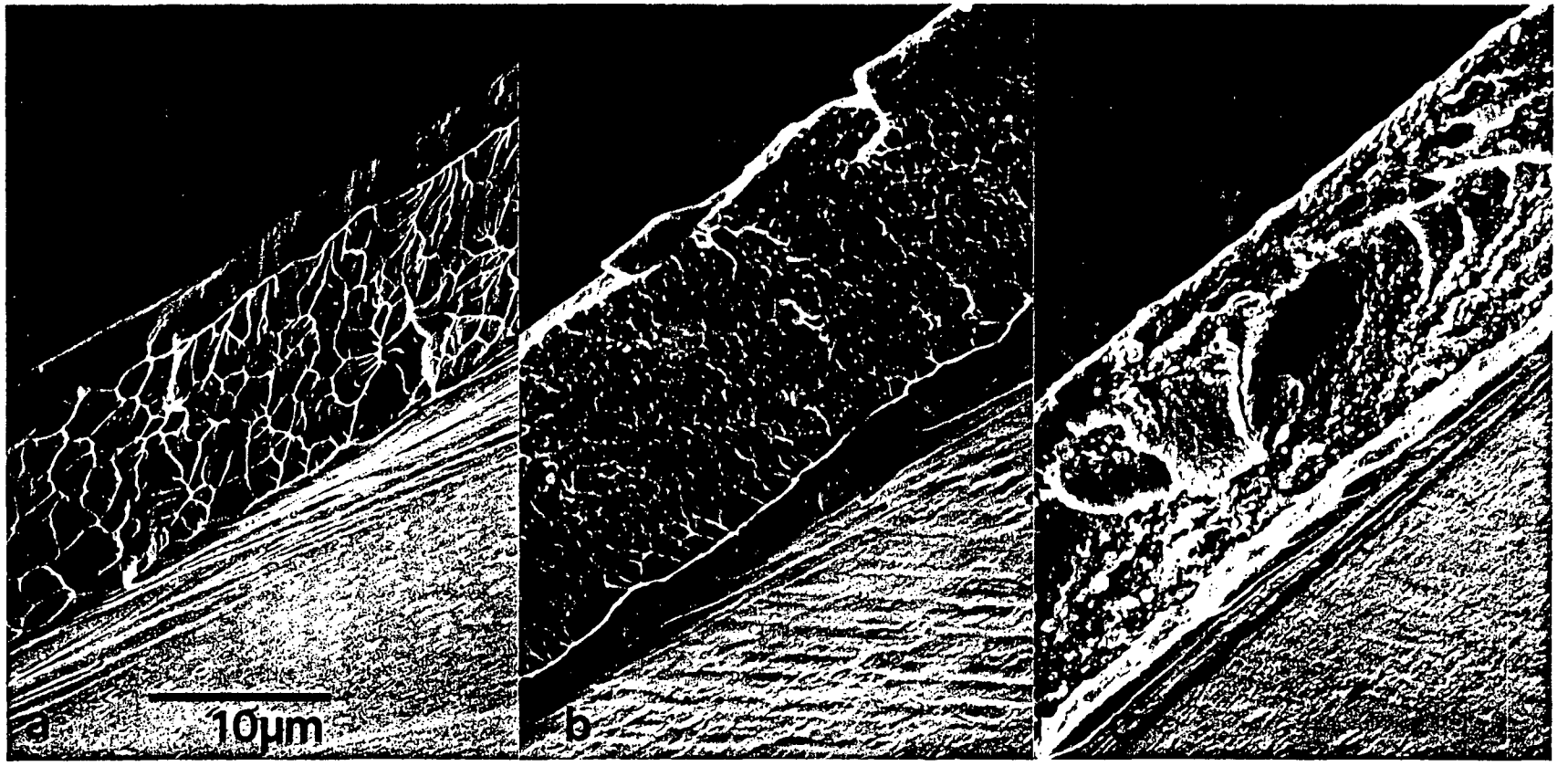

Fig 3 II Merk-Mori-Mori

Fig 4a Merk/Mons/Moris

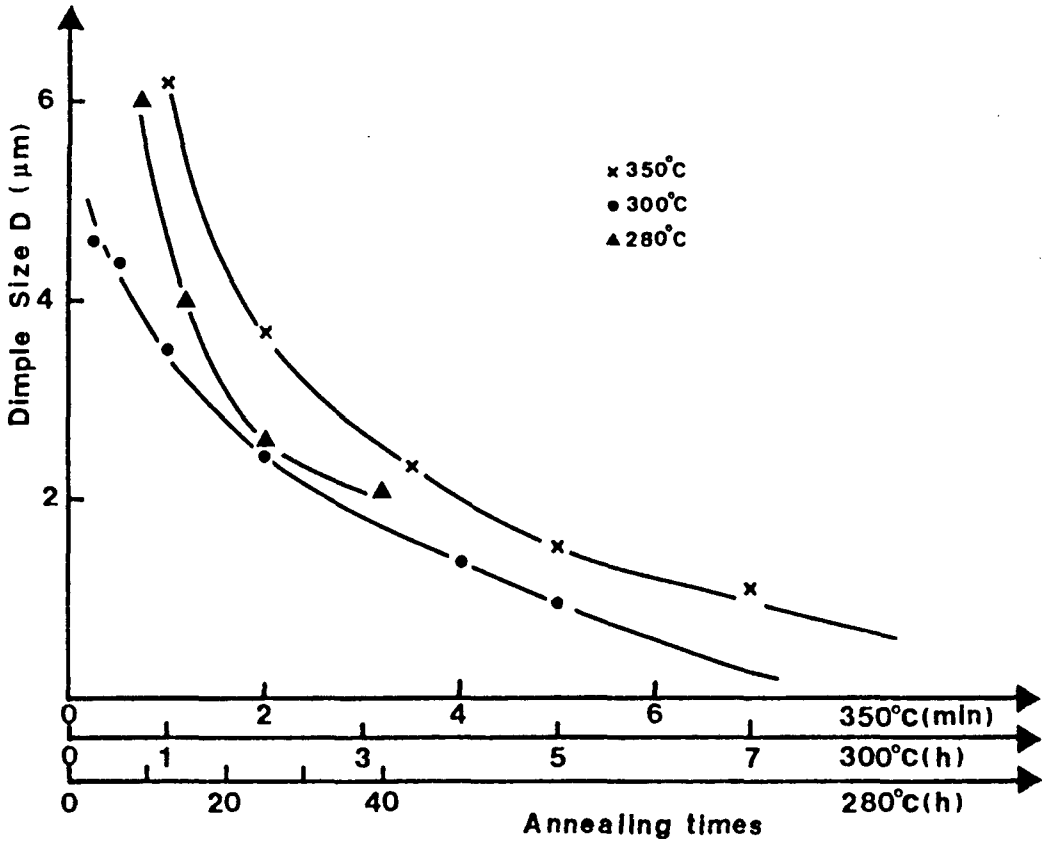

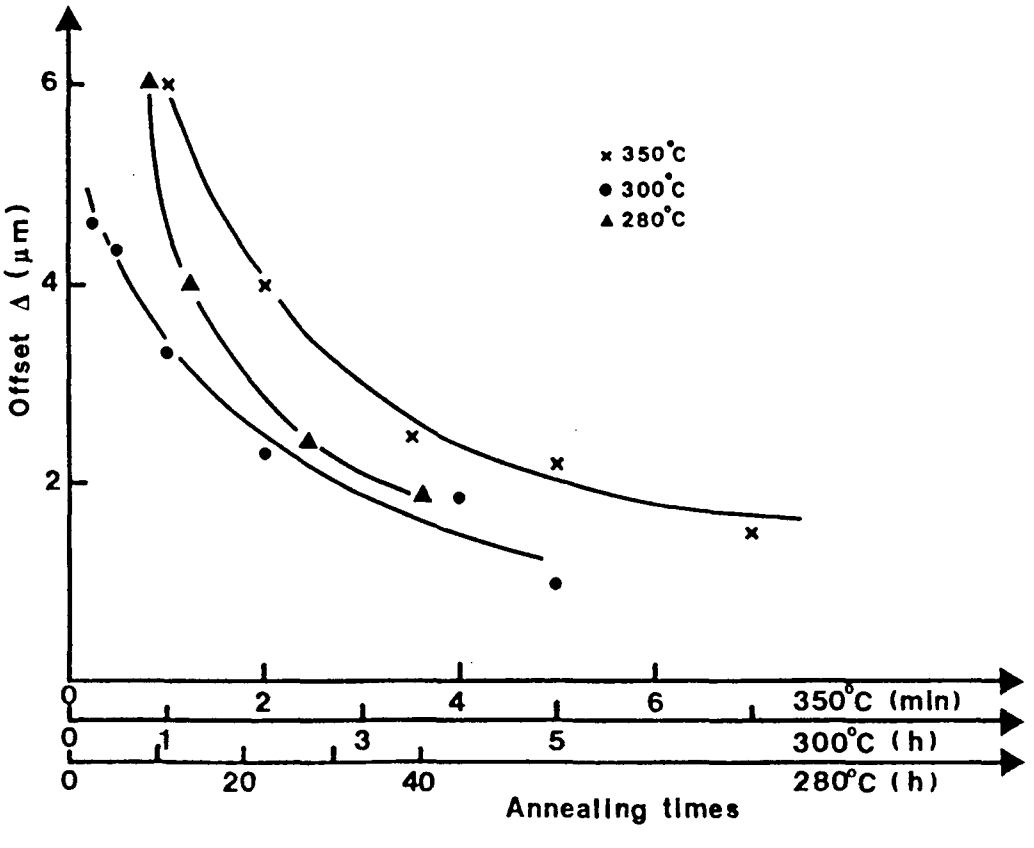

Fig 4 b Mark/Morris/Morris

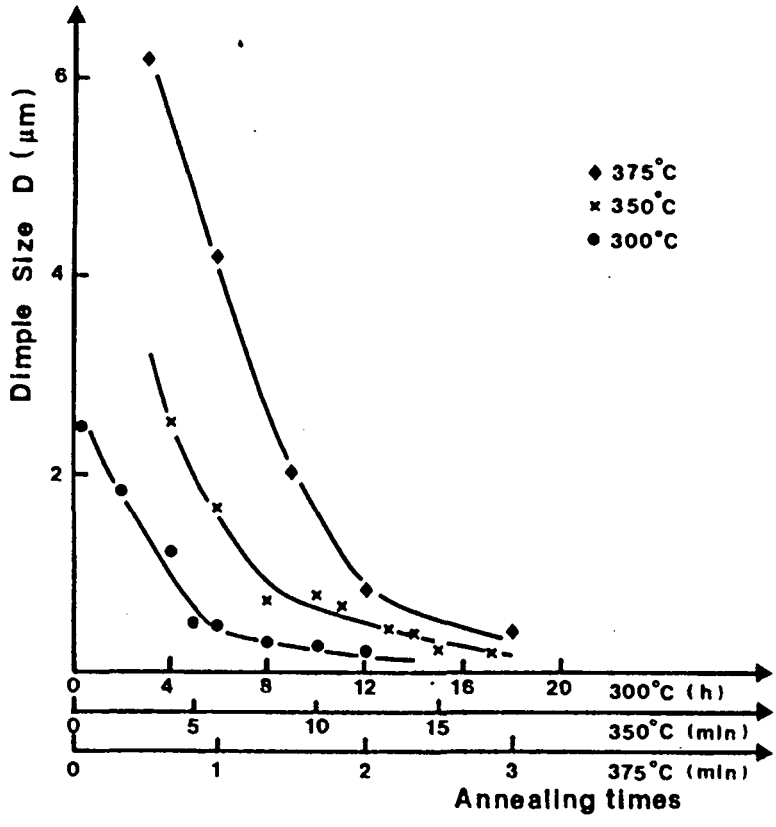

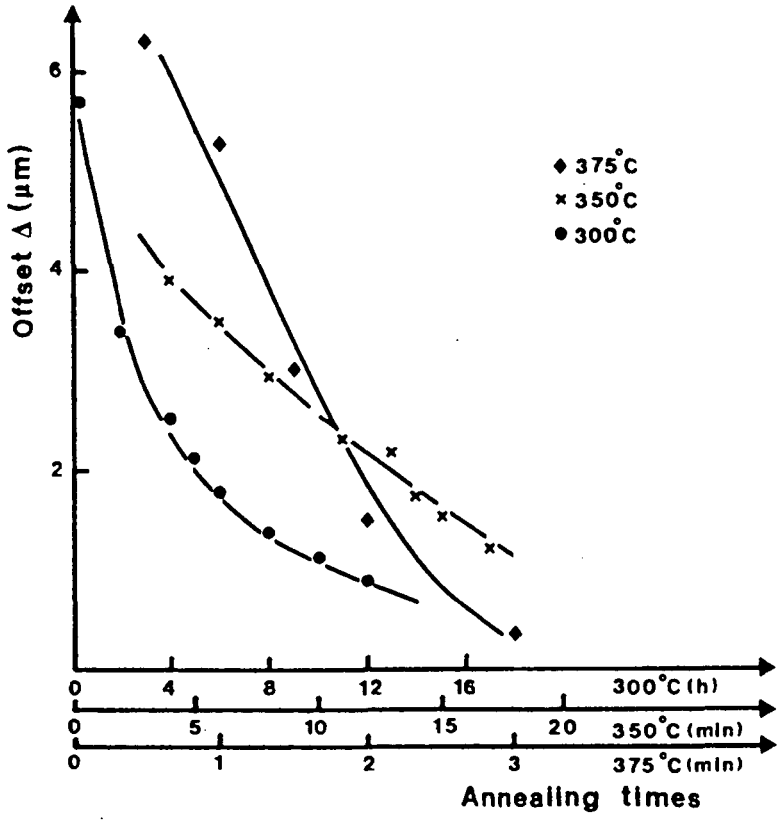

Fig 5a Mark/Mark/Mark

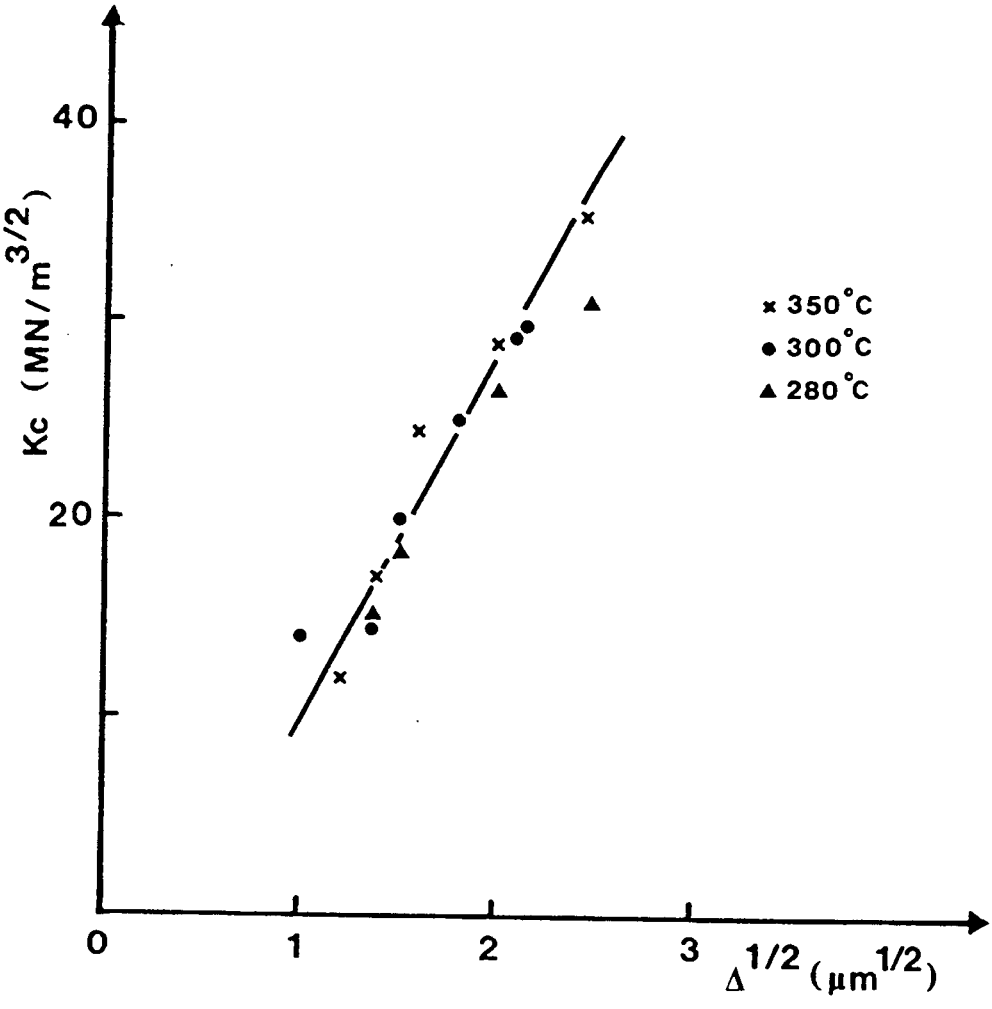

Fig 5b Mark/Morris/Morris

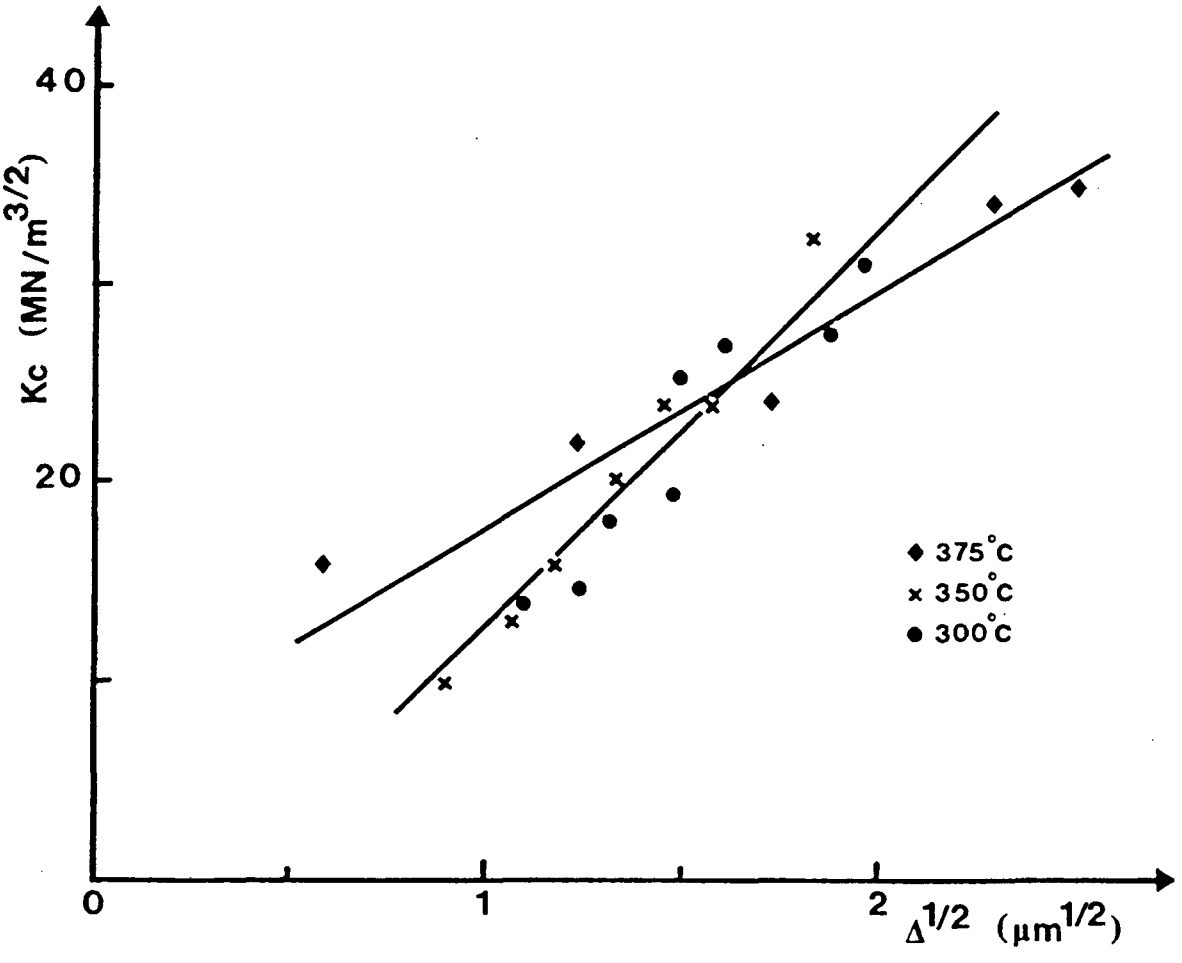

Fig 6 Mark/Morris/Morris

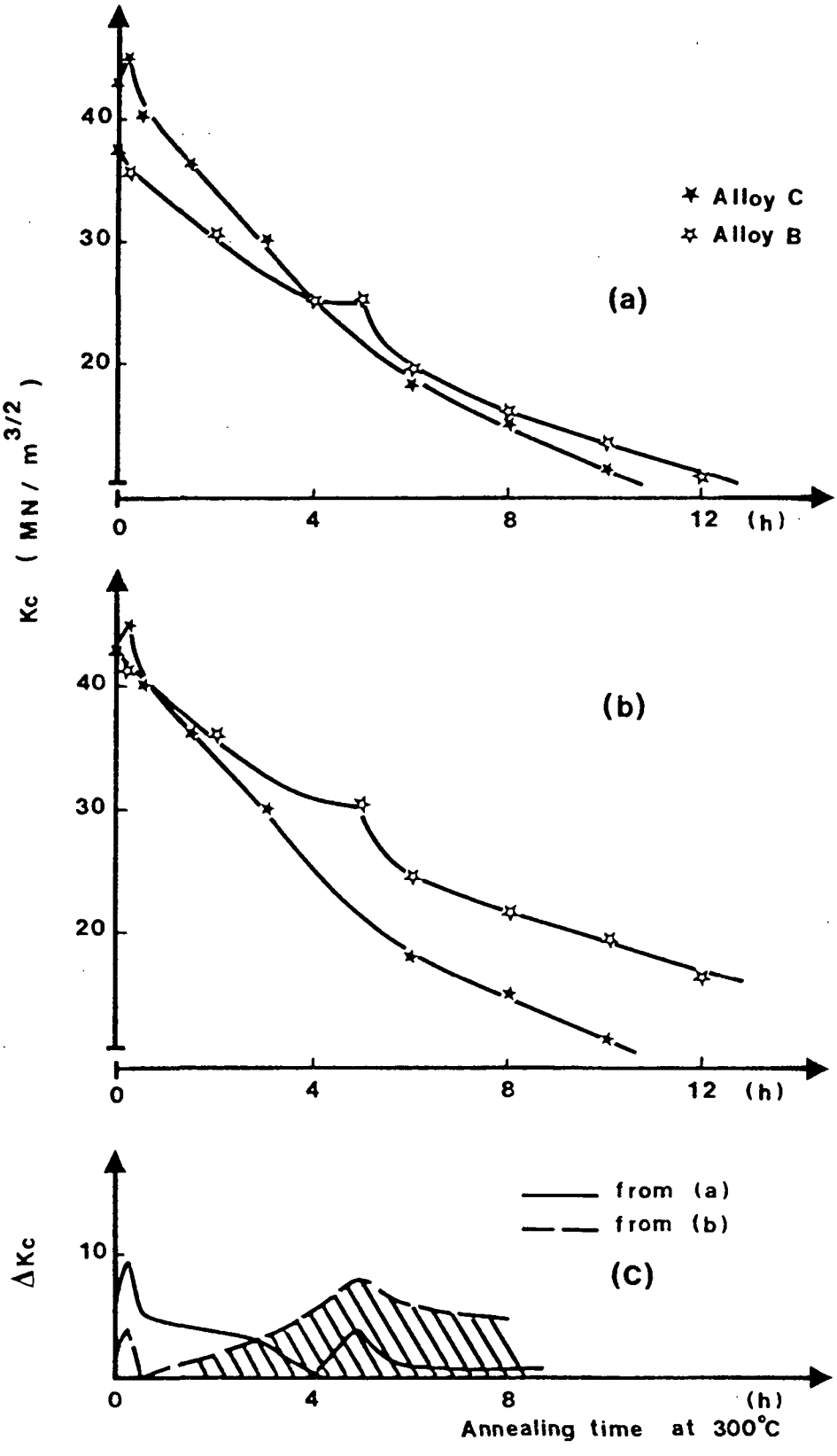

Fig 7 Mech/Morris/Norris

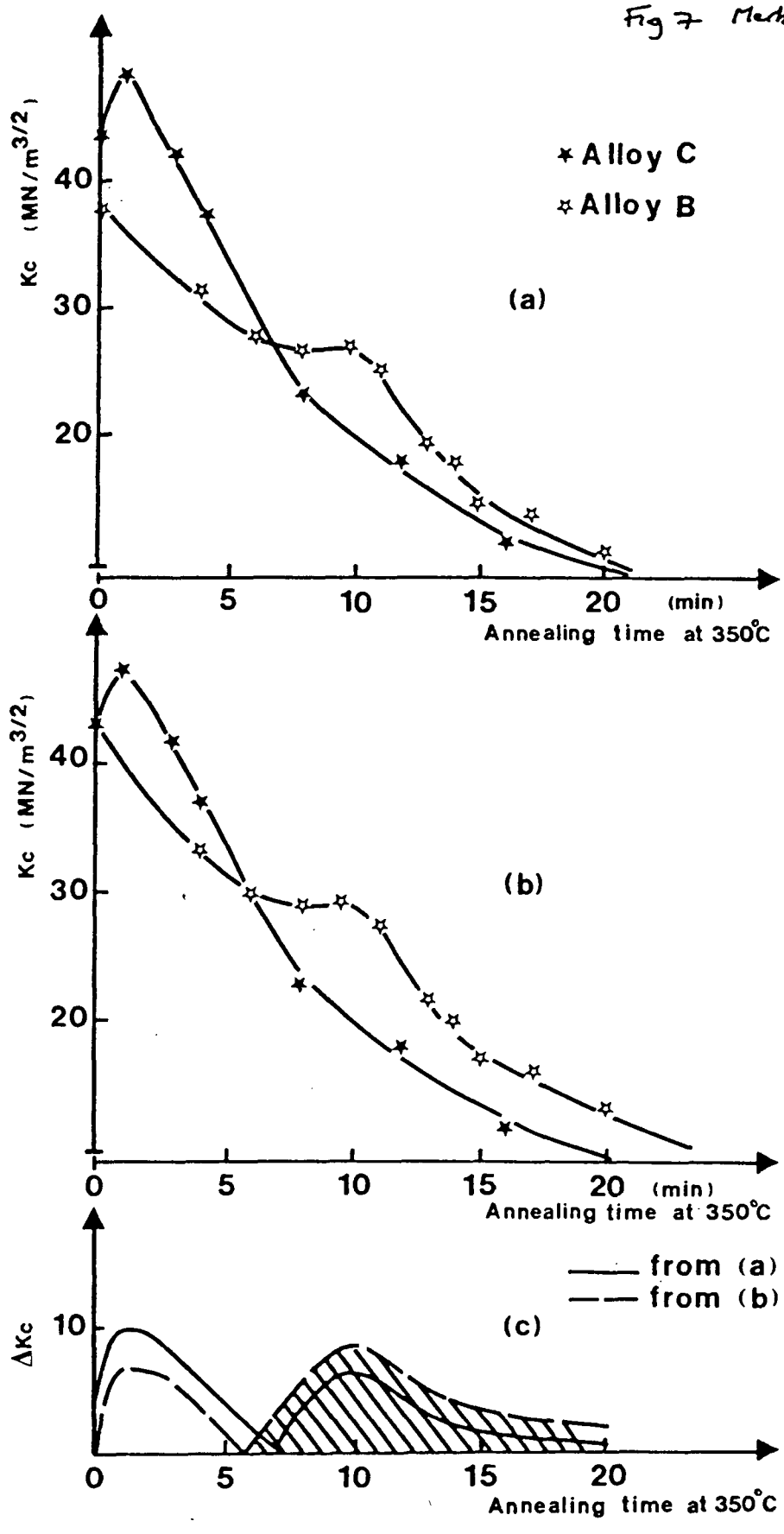

 Submitted J. Mat. Sci

Crystallization Embrittlement of Ni-Ti-B Glasses

D.G. Morris, N. Merk and M.A. Morris,

Institute of Structural Metallurgy, University of Neuchâtel,

CH-2000 Neuchâtel, Switzerland.

Abstract

While metallic glasses have excellent toughness and ductility in the as-cast and unrelaxed state, the process of crystallization leads to a nearly continuous and significant embrittlement. This change is examined on three Ni-Ti-B glasses and related to the morphology and distribution of the crystals obtained.

For the partially-crystallised materials, failure still occurs after intense shear on one well-defined shear plane, and it is shown how the crystals act as stress and strain imcompatibilities causing localised crack or cavity formation. The relationships between sample mechanical properties, fracture surface characteristics and crystal distributions allow an analysis of cavity nucleation and growth rates, and thereby make it possible to suggest microstructures which may maintain reasonable toughness.

Introduction

Metallic glasses are generally characterised by good hardness or strength, as well as significant ductility and toughness (1,2). Plastic deformation occurs by intense shear along well-defined shear planes oriented along the directions of maximum shear stress. During crystallization, however, these materials lose their ductility and become very brittle (3,4). The embrittlement occurring during crystallization is generally understood as caused by the formation of cavities where particles intersect the intense shear band (4,5) in much the same way as for cavity nucleation during the fracture of crystalline materials containing particles (6).

Only on a few occasions, however, have these ideas been examined quantitatively. For example, Zielinksi and Ast (7) have considered the stress concentration at an obstacle at the tip of a shear band, and the applied shear stress (τ^*) necessary to open up a free surface:

$$\tau^* = \left\{ \frac{4\gamma G}{\pi x(1-\nu)} \right\}^{1/2} \qquad (1)$$

where γ is the surface energy, G the shear modulus, ν the Poisson's ratio, and x the length of the shear band. This approach is identical to that for the formation of cleavage cracks in steel (8,9). Substituting in typical values for particle dispersions in a metallic glass, they came to the conclusion that particle cracking could fairly readily be produced for many particles (7). These arguments can in fact be extended to consider, again as has been done for cavity nucleation at particles in crystalline

materials (10), that the stress concentration must be supported by a particle of finite size (Ø) and the stress necessary to cause cavitation or cracking becomes

$$\tau = \tau^* \left\{ \frac{\emptyset}{\lambda} \right\}^{1/2} \qquad (2)$$

where τ^* has the value defined in (1) and λ is the pile-up length, taken as half the separation between the obstructing particles.

Argon has considered the nucleation of cavities at small particles in terms of the plastic deformation necessary to open up the free surface and to cause the cavity to reach a stable size (6,11). According to these arguments, cavity nucleation will be extremely difficult for small amounts of crystallinity when distributed in the form of small (less than 20-25 nm) particles. These ideas are supported by the study of Freed and VanderSande (4) who found that small numbers of small crystals did not lead to significant embrittlement. As such these results correspond to the stage where the ductilisation phenomenon was observed in the prior report (12).

The present work examines the embrittlement occurring during the crystallization of a series of three Nickel-Titanium-Boron metallic glasses. The crystallization behaviour of these materials has previously been reported in detail (13) as well as the fracture toughness variations during crystallization (12). In this previous study it has been shown that the toughness decreases steadily during crystallization, apart from a period of slight ductilisation at the beginning of crystallization explained in terms of slip-band obstruction by the small crystals without yet the

creation of significant extra failure sites. It has also been shown (12) that the fracture surface changes during crystallization, that the shear offset occurring before fracture can be related to the measured toughness value, and that the shear offset and size of dimples on the fracture surface are closely related for a given alloy.

The basic model which will be used to describe the failure of a partially-crystallized material is shown schematically in Fig 1. Shear is considered to take place on a well-defined plane, as observed experimentally. This initial consideration is certainly true for a fully-glassy alloy and remains true as long as the alloy is still mainly glassy, say up to 50 % or so crystallization. The intense shear causes stress and strain concentrations at obstacles in the shear plane leading to localised cavitation or cracking. Such cracks or cavities propagate under the action of the shear deformation until they cover virtually the entire cross-section - failure has occurred. This simplistic model assumes that essentially no normal stress applies across the shear plane. In the typical fracture toughness tests the applied stress was less than one tenth of the tensile strength of the material, and therefore the simple failure criterion seems justified.

It is important to notice that the correlation of fracture surface parameters and particle distribution makes it possible to evaluate the nucleation and growth rates of cavities (or cracks) at particles: this is illustrated with reference to Fig 1. Consider that, at an intermediate stage of failure, the shear displacement is δ and the cavity size d. The relationship of δ to d is related to the growth behaviour of the cavitiy, as

$$\delta = a\, d^n \qquad (3)$$

or, at failure, as

$$\Delta = a\, D^n \qquad (4)$$

where Δ and D are the shear offset and dimple size measured on the fracture surface. For example, assuming that cavity growth occurs at the same rate as the shear, and that a nucleation shear (c) was necessary to form the cavity, we obtain

$$\Delta = D + c \qquad (5)$$

In an analogous way, information on the nucleation kinetics will be obtained from the relationship between the final cavity size (dimple size) and the spacing between the crystalline particles (λ) (or (λ-$\emptyset$) if the particle size ($\emptyset$) is important). In this way the relationship

$$D = m\,(\lambda - \emptyset) + p \qquad (6)$$

suggests an incubation term associated with nucleation (the term p) and the likelihood of cavity formation at a given particle as 1/m. Thus, in Fig 1, the value of n is 2 since one half the particles lead to cavitation.

The number of particles of size $\emptyset$ intersecting a given plane is

$$N_p = \frac{\emptyset}{\lambda^3} \qquad (7)$$

This expression is applicable in the present case provided the shear band thickness is less than the particle size. Estimates of the shear band thickness have been given as 10-20 nm (3), while the particle sizes range from 30 nm at the point where crystallization embrittlement begins to above 200 nm. Assuming that a fraction f of particles leads to cavitation, the

number of cavities per unit area is

$$N_C = f\ \frac{\emptyset}{\lambda^3} \qquad (8)$$

and considering that this fraction depends inversely on the ratio $\emptyset/\lambda$, as suggested in equation (2), we have

$$N_C = g\left(\frac{\lambda}{\emptyset}\right)\ \frac{\emptyset}{\lambda^3} = \frac{g}{\lambda^2} \qquad (9)$$

The dimple size at failure would then, simply, be

$$D = N_C^{-1/2} = \lambda/\sqrt{g} \qquad (10)$$

It is clear from the relationships developed here that a detailed study of shear offsets, cavity (dimple) sizes and spacings of cavities and particles will be useful for learning about nucleation and growth rates during the shear and failure of partially-crystallized alloys. It is clear that, ideally, these rates should be determined on a given material as different amounts of shear are accumulated and as fracture approaches. In the present work an easier approach has been taken, namely of assuming an equivalence of the nucleation and growth rates of differently heat-treated material, and examining the fracture surfaces only. This is equivalent to considering that the material-dependent terms (a,n,c,m,p,f and g in equations 3-10) are alloy dependent but not heat-treatment dependent. While not precisely correct, this does not seem an unreasonable supposition, at least for a first analysis.

Experimental Details

The three alloys examined were the same as those treated in the preceding paper (12), namely $Ni\text{-}B_{19.1}Ti_{2.1}$ (alloy A), $Ni\text{-}B_{18.2}Ti_{3.8}$ (alloy B) and $Ni\text{-}B_{17.9}Ti_3$ (alloy C), where details of heat treatments and mechanical testing procedure were also given. It should be recalled that alloy A crystallizes by the formation of a few, large eutectic colonies, alloy B by forming many, small τ phase crystals, and alloy C a mixture of both types. Following failure, the fracture surfaces were examined using a Cambridge 250 Scanning Electron Microscope. In addition, shear band and crack interactions with particles were examined using Transmission Electron Microscopy. Shear band interactions with particles were studied after slightly bending the partially-crystallized material. Thin foils were then prepared from either the tensile side or the compressive side of the bent sample by blanking off one of the acid jets in a twin-jet electropolishing device and thereby electropolishing only from the opposite side. Crack interactions with particles were examined on lightly-deformed thin-foil samples: a number of cracks was always found running from the edge of the electron-transparent areas into the thicker areas of the foils.

Results

According to the model outlined in Fig 1, as crystallization takes place and the sites where cavitation may occur during deformation become more numerous, as fracture toughness decreases the number of cavities or dimples on the failure surface should increase and accordingly the dimple size and failure offset decrease. This is clearly illustrated in Fig 2. During crystallization both the amount of shear offset and the dimple size decrease (Fig 2a and b). This effect depends on the distribution of the

particular particles present, as seen in Fig 2c and d, where the finer dimple size is seen to correspond to the alloy containing many small τ phase particles rather than fewer, larger eutectic particles. This relationship between cavity nucleation, dimple formation and final failure is well illustrated in Fig. 3. Many of the dimples seen are clearly associated with small cracks or cavities which may have formed because of a crystalline particle. In addition, in this Figure, it is clear that the cavities have grown to cover essentially the entire surface before the remaining ligaments are torn out during the final tensile stage of failure.

Quantitative relationships between the fracture surface parameters and crystal distributions are illustrated in Figs 4-6 and summarised in Table I. In Fig 4 it is seen that the shear offset before failure (Δ) and the average dimple size (D) are related linearly (in fact a one-to-one relationship) for the alloy A and by a parabolic relationship for alloy C: alloy B showed the same parabolic relationsship as alloy C. These relationsships correspond to those outlined in equations 4) and 5), with an intercept close to zero in each case: the values of the slopes of the lines obtained at each temperature are given in Table I. Relationships between the dimple size and the distribution of crystalline particles are illustrated in Fig 5. For alloy A, Fig 5a, there is a linear dependence between the dimple size and the interparticle spacing, expressed as (λ-$\emptyset$) where λ is the spacing between particles and $\emptyset$ the particle size. The slope of the line varies with temperature, as reported in Table I. For alloy B, Fig 5b, a similar dependence is observed, but better described directly in terms of the interparticle spacing λ. Again Table I shows that the slopes of the lines are temperature dependent. It should be noted that the linear

relationship between D and λ is in agreement with the relationship of equation (10), also showing some nucleation or growth incubation effect. For alloy C two possible relationships between D and λ may be found, taking account of only the few, large eutectic particles present, or taking account of all the particles. For both a reasonable linear relationship is obtained, reported in Table I, and it is not possible to decide a preference for one relationship or other.

From the relationships between shear offset and dimple size, and between dimple size and particle spacing, it is clear that a relationship exists between shear offset and particle spacing. This is shown in Fig 6 for the alloys A and B and the relationships are summarised in Table I for the three alloys. For the alloy C three possible relationships are indicated, one related to the large eutectic particles and two related to the many small particles (the scatter in data points prohibits a precise distinction between one or the other). Overall it can be seen that alloy C most closely resembles alloy B in its fracture behaviour, and hence it appears that the many, small τ particles present in the alloy C are more important in determining fracture than the fewer, larger eutectic particles.

Interactions between cracks formed in thin foils and the particles present are useful in giving an overall impression of the influence of these particles, even if the different stress conditions during tearing the thin foil and during fracture toughness testing the melt-spun ribbon prohibit a precise comparison. Such interactions between particles and cracks are shown in Fig 7. In Fig 7 a it is seen that the large eutectic particles are often cracked, and often lead to a significant deviation of the crack path. It is interesting to note, however, that many of the particles do not

crack, but simply deviate the propagating crack along the particle-matrix interface. As illustrated here, it is particularly those particles with their long axes perpendicular to the crack which tend most readily to crack. Fig 7b illustrates a typical crack making its way through a glass containing many τ-phase particles. It is extremely rare, here, to find a particle which has obviously cracked or caused cavitation. More generally the crack follows the particle-matrix interface, apparently deviating around each particle encountered as the crack propagates.

Further information can be obtained from shear band interactions with particles before failure has occurred. This has been possible by studying the thin foils prepared on already-deformed, partially-crystalline material. Of particular interest here is an estimation of the influence of long-range stresses and interactions. For example, the increased density of the crystalline phase may cause a tensile hydrostatic field around the particle, or the cooling process following annealing may cause a compressive field because of the greater thermal dilation of the glassy matrix (7,14). As a result of such stress fields, Donovan (15) has reported shear bands deviating towards or away from particles before direct contact occurs. As seen in Fig 8, there is no evidence of such long range interaction for the present alloys, neither around the large eutectic particles (A) nor around the small τ-phase particles (B). Exactly the same results were obtained on the tensile and on the compressive side of the bent samples. As such, we can correctly consider that a shear band will only interact with a particle if this lies directly in the shear plane, and the development of equations (7)-(10) is supported.

Figs 9 and 10 show shear bands interacting with small crystalline particles where the beginning of cavitation is visible. In both cases it appears that cavitation has started within the particles rather than at the particle-matrix interface, although it is difficult to be certain about this. It is, however, clear that fracture processes are initiated at the particles and thus it is the interaction of the shear band with these particles which is responsible for the embrittlement of the glass during crystallization.

Discussion

The fracture model outlined in the introduction was based on crack or cavity nucleation where an intense shear band intercepted crystalline particles, followed by the shear-controlled growth of these cavities to near-complete coverage of the shear plane, and then failure in tension. It was shown how an examination of the distribution of the crystalline particles could be related to the fracture morphology to deduce information on cavity nucleation and growth. The results presented here have verified the model, and as well allow a discussion on the cavity behaviour. Thus, it has been shown that cavity nucleation indeed takes place where the shear band meets the particle, and that only some of the particles will actually crack or caviatate. It has also been shown that the shear band is not affected by long range elastic interactions which may exist around particles, and therefore the shear band - particle intersection probability can be treated purely on geometrical grounds. Finally, fracture has been shown to occur when the cavities have grown to cover a very significant fraction of the shear plane. We shall now proceed to a quantitative evaluation of cavity nucleation and growth rates at different types of particles.

According to equations (4) and (5), the growth dependence of cavities may be deduced from the generalised formula

$$\Delta = a\, D^n + c \qquad (11)$$

It should be mentioned here that the growth of cavities is implicitly assumed to depend on the shear strain, that is on plastic deformation, rather than being time, or diffusion, dependent. In view of the very high strain rates occurring within the shear bands (values in excess of 10^2 - 10^3/s can be deduced from the work of Neuhauser (16)) this seems a reasonable supposition. The value of c in equation (11) represents an incubation shear displacement necessary to create a growing cavity: as seen from Table I this parameter has a value of zero indicating that nucleation and growth take place already from the very start of shear. For alloy A, containing the large eutectic particles, the values on n and a are unitiy (see Table I) such that cavity growth occurs at exactly the same rate as the shear displacment. For alloy B, containing the small τ-phase particles (alloy C behaves in the same way as alloy B) there is a parabolic relationship between Δ and D, see Table I. This in fact means that the initial growth rate of the very small cavities, associated with the very small particles, is very slow and later accelerates to about the same rate as for the large cavities associated with the large eutectic particles - this is illustrated in Table II showing the estimated cavity sizes for the two alloys A and B after different amounts of shear strain. It would seem, therefore, that cavity growth at very small sizes may be difficult, probably because of a tendency for plastic flow around a small particle and a tendency of cavity re-healing much as described by Argon for very small cavities (6), whilst for large cavities and large particles (eutectic particles) there is little tendency to rehealing and cavity growth is a direct, shear-induced tearing process.

Cavity nucleation at particles may be examined in terms of equations (6) and (10), relating the cavity size, or dimple size, to the interparticle size. It is clear here that the situation of a large particle cracking and creating already a large crack, or of a small cavity nucleating and growing slowly at a particle are two different cases, and equation (10) may need to be modified as

$$D = (\lambda - \emptyset)/\sqrt{g} \qquad (12)$$

to consider the situation where the cavity needs only to grow over the glassy matrix between the cracked particles. The experimental data, summarised in Table I, are shown to fit these relationships (equations (10) or (12)). The relatively large scatter in the data does not allow further discussion of a preference for one of these two relationships. Equally, the nucleation data for alloy C, which may be interpreted either in terms of the large, eutectic particles or in terms of the small, τ phase particles, does not allow a distinction of better experimental fit to one or other data set nor a selection of the important particle species to be made. However, based on the observation of cavity growth rate for this alloy depending on the small, τ phase particles, exactly as for alloy B, we note that cavity nucleation behaviour of alloy C can be sufficiently well interpreted in terms of these small particles.

The parameter g of equations (9), (10) and (12) has a value of near 0.1 for alloy A and 0.01 for alloy B (also for alloy C). Accordingly, for a given alloy and heat treatment, we can say that the fraction (f) of particles which will crack or cause cavities is 0.1 $\lambda/\emptyset$ for alloy A and 0.01 $\lambda/\emptyset$ for alloys B and C (see equations (8) - (9)). During the course of crystallization the value of $\lambda/\emptyset$ will vary from very high, say ~10 at the

beginning of crystallization as embrittlement begins ($\lambda/\emptyset$ ~10 implies ~0.1 % crystalline volume), to less than 2 for the heavily embrittled materials. The fraction of particles causing cavities thus varies from say 100 % to 10 % for the large, eutectic particles, and say 10 % to 1 % for the small, τ phase particles.

These deductions would appear to be in good accord with the observations on shear bands and cracks in thin foils: only a relatively small fraction of particles encountered by a shear band actually cracks or causes a cavity to nucleate (the other particles may deviate the shear band slightly or deform with the matrix, in part dependent on the relative orientation of the shear band and the crystalline particle); the fraction of particles nucleating damage in this way is significantly larger for the eutectic particles than for the τ phase particles (it is not known whether this is a size effect - larger particles are inherently more susceptible to crack - or may arise because of the particular phase nature or presence of interphase boundaries within the eutectic particles); finally a cracking probability dependent on $\lambda/\emptyset$ is exactly that expected from equation (2).

The final relationships reported in Table I, namely those relating the shear offset and the interparticle spacing, are clearly the consequence of a given growth dependence and a given nucleation rate dependence. The relationships (Δ-λ) may thus be regarded as important fracture criteria, relating the given microstructure (λ,$\emptyset$) to the fracture toughness (Δ). However, no additional information on the failure process can be learned, since these relationships are clearly the products of the nucleation (D-λ) and growth (Δ-D) expressions.

Finally, based on the understanding gained of failure mechanisms in partially-crystalline metallic glasses, it is interesting to speculate on best ways of limiting the embrittlement caused by the addition of crystals. This question is of particular interest in view of the development of techniques for reinforcing glasses with a cast-in dispersion of particles (17) and of controlling magnetisation stresses by selective crystallization (18).

According to the present analysis, we can distinguish three parameters pertaining to the crystalline particle distribution which affect fracture: particle nature, ratio of particle size to spacing, and actual values of particle sizes and spacings. The first of these parameters depends on the degree of inherent crack resistance of the particle and the particle interface nature. The single-phase τ particles are clearly superior to the complex, eutectic phase particles in the present study. In this sense the strong TiC or WC particles used for dispersion-strengthening studies (eg 17) appear well chosen. The ratio of particle size to spacing ($\emptyset/\lambda$) is important because it controls the stress concentration at the particles and helps determine the probability of cracking or cavitation. To limit damage this ratio should be as large as possible, hence implying a large volume fraction of crystalline material. Thirdly, the actual sizes of the particles should be large, implying a large interparticle spacing for the selected volume fraction crystalline. In this way the distance over which cavities must grow before final failure occurs will be maximised.

Acknowledgements

One of us (NM) is grateful for financial support from the Swiss Commission for the Encouragement of Research (Project No 1322) and the Swiss National Science Foundation (Project No 2.022-0.86) during this work.

Conclusions

The fracture behaviour of partially-crystalline samples has been examined based on a model of intense shear within a localised shear band causing cavity nucleation and growth where this band intercepts a crystalline particle. Failure is considered to occur under the action of relatively minor normal stresses when the cavities cover a large fraction of the shear plane.

A careful comparison of the fracture surface morhology with the distribution of the crystalline particles makes it possible to deduce the nucleation and growth rate of the cavities. The fraction of particles causing damage is relatively small, as confirmed by examination of shear bands and cracks in thin foil samples by transmission electron microscopy, and dependent on the type of particle and the ratio of size to spacing. The growth rate of the cavities also depends on the nature of the particle causing caviation: large cavities associated with large eutectic particles grow at the same rate as the shear displacement, whilst the small cavities formed at small τ-phase particles grow initially very slowly and later at the same rate as the eutectic-cavities - the difference in cavity growth behaviour may be purely size dependent, caused by the difficulty of cavity growth at very small sizes.

The improved understanding of failure processes in these materials allows a prediction of optimum microstructure for increasing toughness by: (i) selecting particles which are strong and well-bonded to the matrix (here the single phase τ particles are preferable to the eutectic phase mixture particles); (ii) selecting a large volume fraction crystallinity to limit stress concentrations at any one particle; and (iii) by selecting large particles, widely separated, such that the cavity growth distance before failure is considerable.

Table I

Relationships observed between shear offset on fracture surface (Δ), dimple size (D) and particle spacing (λ or $\lambda-\emptyset$)

Alloy	Relation	Value of slope (a, m or b)				
		260 °C	280 °C	300 °C	350 °C	375 °C
A	$\Delta=aD$	-	1.05	0.86	0.9	-
	$D=m(\lambda-\emptyset)+p$	-	6.4	2.6	1.7	-
	$\Delta=b(\lambda-\emptyset)+d$	-	4.1	2.3	1.5	-
B	$\Delta=aD^{1}/_{2}$	-	-	2.3	2.3	3.2
	$D=m(\lambda-\lambda_0)$	-	-	6	11.8	11.7
	$\Delta=b\lambda^{1}/_{2}+d$	-	-	9	14	13
C	$\Delta=aD^{1}/_{2}$	2.2	-	2.15	2.4	-
	$D=m(\lambda-\emptyset)+p$					
	(τ particles only)	13	-	16	9	-
	(eutectics only)	1.3	-	3.6	2.8	-
	$\Delta=b(\lambda-\emptyset)^{1}/_{2}+d$					
	(τ particles only)	9	-	13	9	-
	(eutectics only)	2.5	-	6.6	4.3	-
	$\Delta=b(\lambda)^{1}/_{2}+d$					
	(τ particles only)	12	-	20	11	-

References

1. H. Kimura and T. Masumoto, in Amorphous Metallic Alloys, Ed. F.E. Luborsky, Butterworths, London, 1983, p 187.

2. L.A. Davies, in Metallic Glasses, ASM, Metals Park, Ohio, 1978, p 191.

3. T. Masumoto and R. Maddin, Acta Met. 19 (1971) p 725.

4. R.L. Freed and J.B. VanderSande, Acta Met. 28 (1980) p 103.

5. C.A. Pampillo, J. Mat.Sci. 10 (1975) p 1194.

6. A.S. Argon, J.Im and R. Safoglu, Met. Trans. 64 (1975) p 825.

7. P.G. Zielinski and D.G. Ast, Acta Met. 32 (1984) p 397.

8. E. Smith, in Physical Basis of Yield and Fracture, Conf.Proc. p 36, Inst. Phys.Soc., Oxford (1966).

9. E. Smith, Metal Sci.Journal, 1 (1967) p 56.

10. E. Smith, Metal Sci.Journal 1 (1967), p 1.

11. A.S. Argon, J.Eng.Mater.Tech. 98 (1976) p 60.

12. N. Merk, D.G. Morris and M.A. Morris, J.Mat.Sci., preceding publication.

13. N. Merk, D.G. Morris and P. Stadelmann, Acta Met., in press.

14. G. Gerard and A.C. Gilbert, J.Appl.Mech. (ASME) 24, (1957) p 355.

15. P.E. Donovan, Mat.Res.Soc. Symp.Proc. 28 (1984) p 197.

16. H. Neuhauser, Scripta Met. 12 (1978) p 471.

17. H. Kimura, T. Masumoto and D.G. Ast, Acta Met. 35 (1987) p 1757.

18. H.R. Hilzinger and G. Herzer, Proc. 6th Int.Conf. on Rapidly Quenched Metals, Montreal 1987, in press.

Figure Captions

Fig. 1. Illustration of the fracture model used in the present analysis. Shear along a direction of high shear stress causes cavity nucleation and growth at particles on the shear band. Failure occurs when the cavities cover essentially the entire cross-section giving rise to the characteristic shear offset and dimpled fracture surface.

Fig. 2. Scanning electron micrographs illustrating the influence of different amounts of crystallization (a-b) and different sizes and distributions of crystals (c-d) on fracture surface morphology:
(a) alloy C after 2 h at 300 °C, about 0.2 % crystallized;
(b) alloy C after 3 h at 300 °C, about 1.5 % crystallized;
(c) alloy A after 2 min at 350 °C, about 0.5 % crystallized;
(d) alloy B after 11 min at 350 °C, about 0.5 % crystallized.

Fig. 3. Fracture surface from partially crystallized sample showing that many of the dimples originated at cracked or cavitated inhomogeneities, presumably particles. During final fracture the remaining ligaments are pulled out. Alloy A after 3 1/2 min at 350 °C.

Fig. 4. Relationships between shear offset at failure (Δ) and dimple size on the fracture surfaces of samples of (a) alloy A and (b) alloy C.

Fig. 5. Relationships between dimple size on the fracture surface (D) and average spacing between particles within the material (λ). a and b are the dimensions of the elliptical eutectoid particles. (a) alloy A and (b) alloy B.

fig. 6. Relationships between fracture offset and particle spacing (λ or λ-Ø): (a) alloy A and (b) alloy B. (a and b are the dimensions of the elliptical eutectoid particles).

Fig. 7. Cracks formed in partially-crystallized thin foils (transmission electron micrographs). A few of the eutectic particles (a) are cracked, while the τ-phase particles (b) deviate the crack around the particle-matrix interface: (a) alloy A after 24 h at 280 °C, (b) alloy B after 13 mins at 350 °C.

Fig. 8. Shear bands in a slightly-bent sample containing both eutectic and τ-phase crystals. Thin foil for transmission microscopy was prepared from the tensile-stress side of the bent sample. Alloy C, after 6 min at 350 °C.

Fig. 9. Shear band intersecting small eutectic particles leading to fine cavitation, apparently within the particles rather than at the particle-matrix interface.

Fig.10. Shear band interesecting small particle in alloy B. The low magnification picture shows the shear band running from the edge of the foil through the particle. The higher magnification picture shows clearly the small cavity formed at the particle.

Fig 1 Morris - Meth-Morris

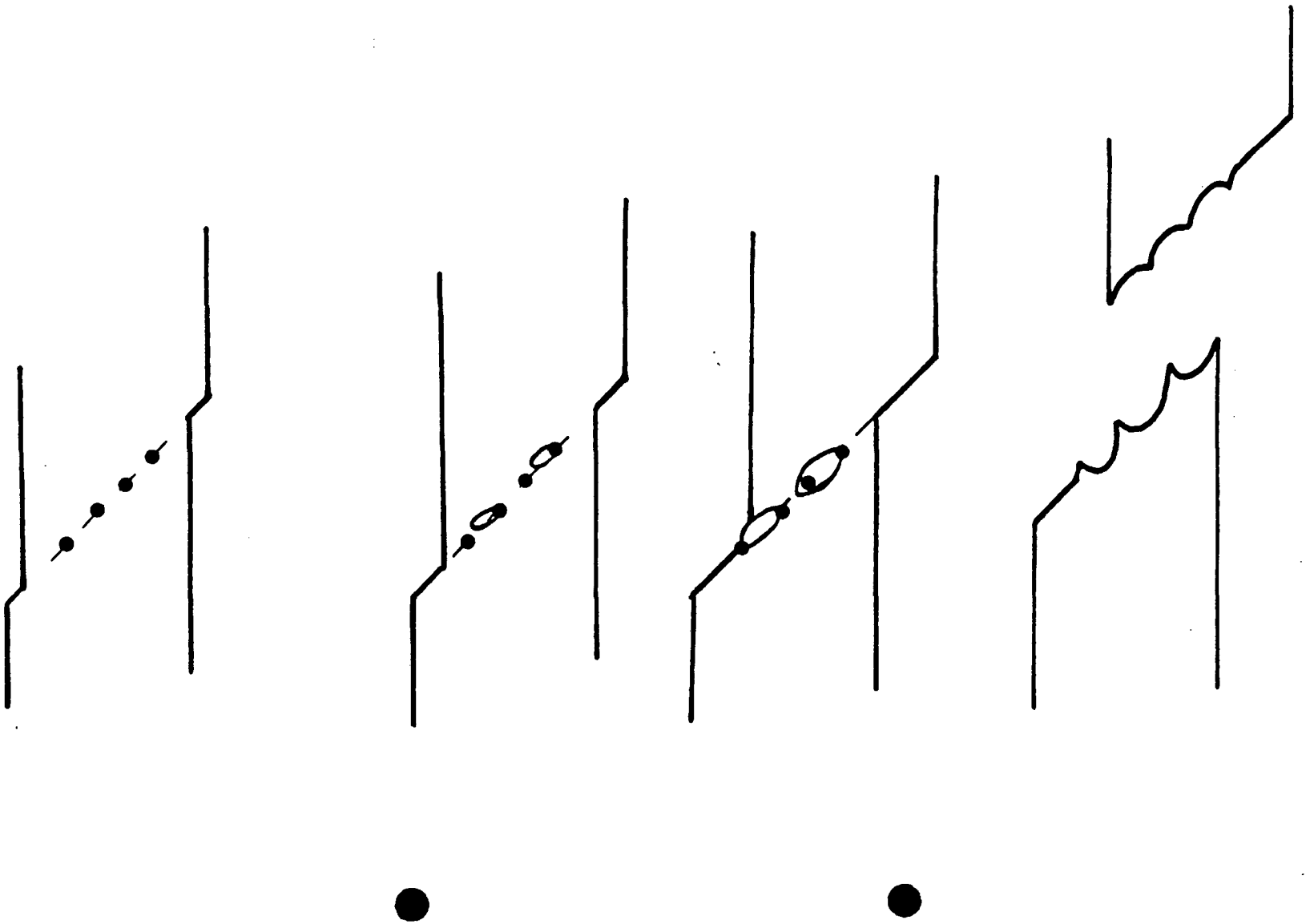

Fig 2 Morris-Mok-Morris

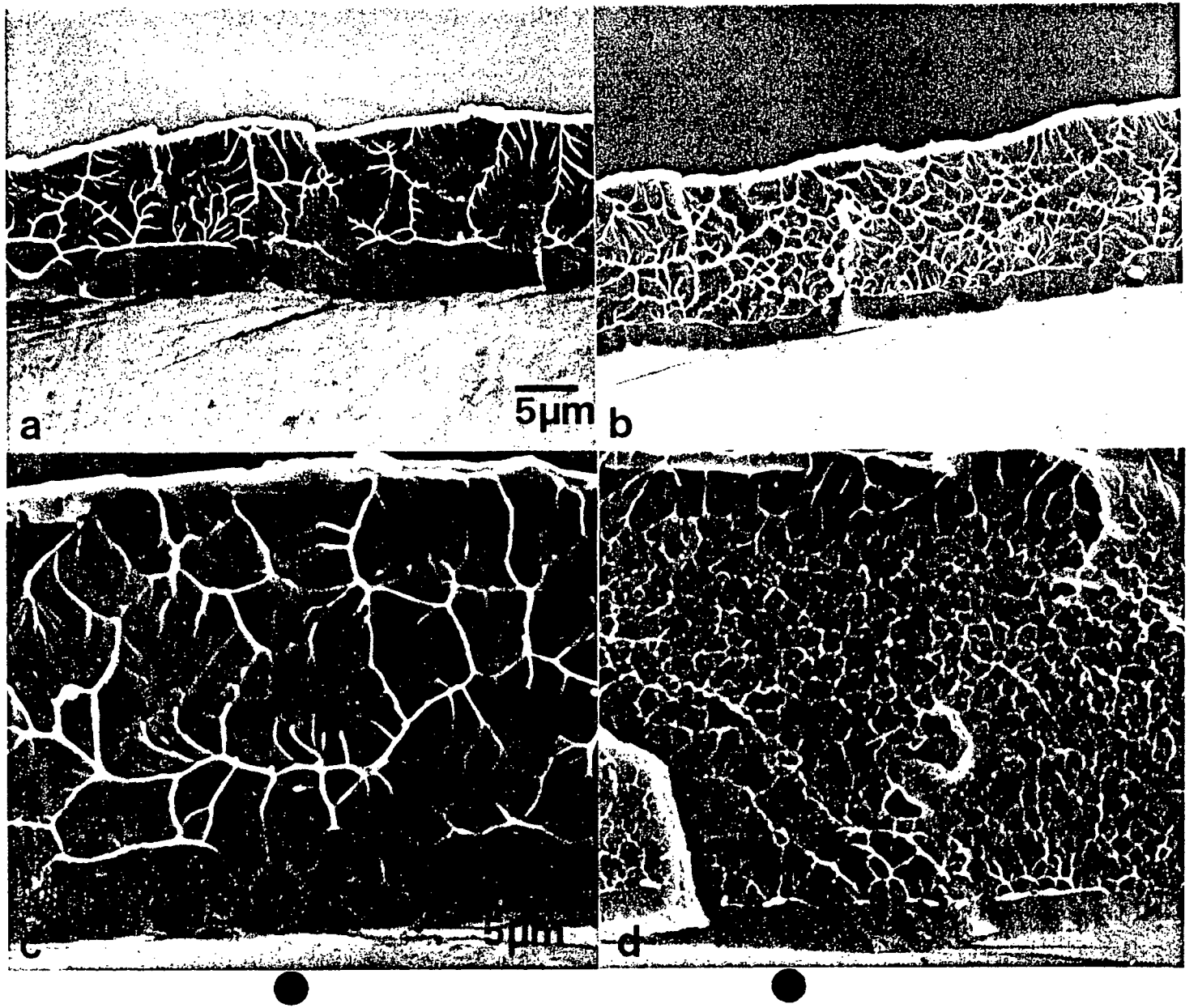

Fig 3

Morris-Merk-Morris

Mons-Marth-Momi

Fig 4a

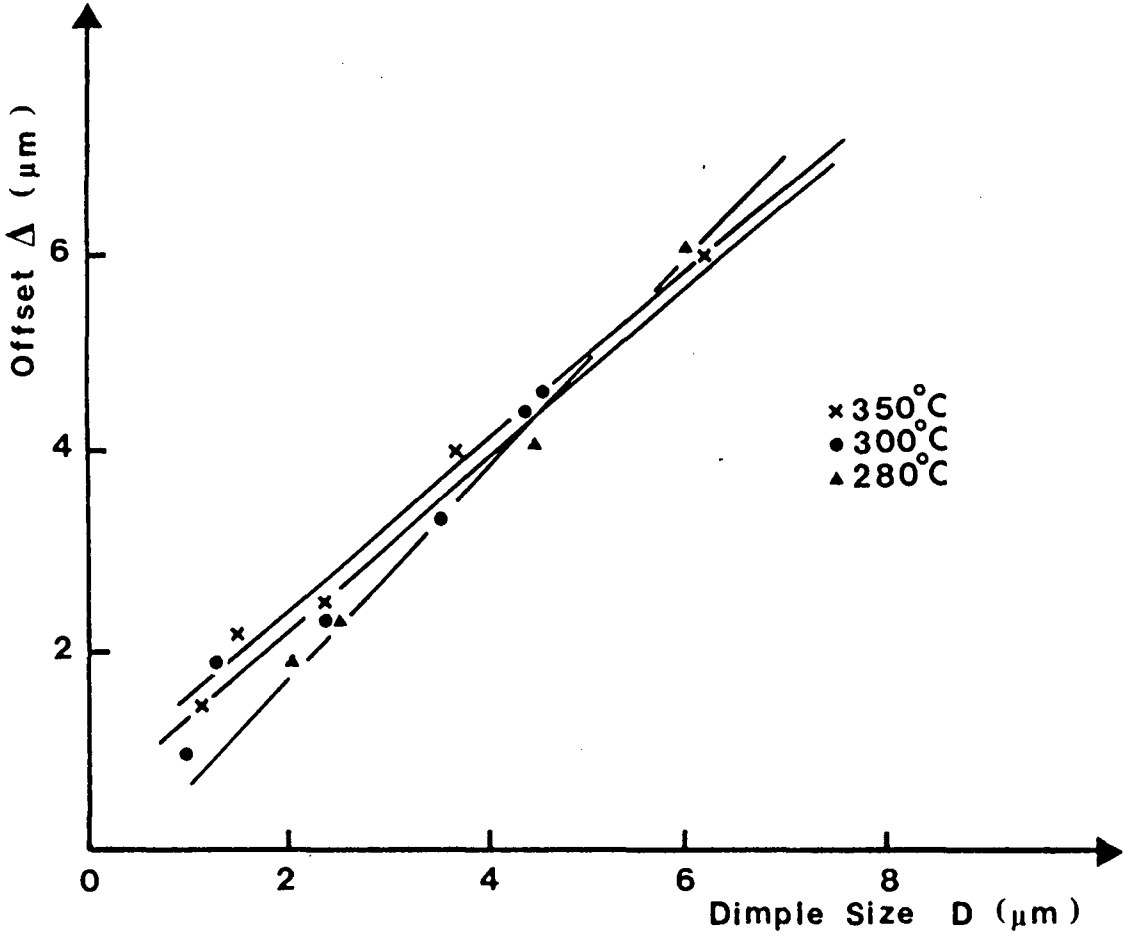

Morin-Merh-Morin

Fig 4b

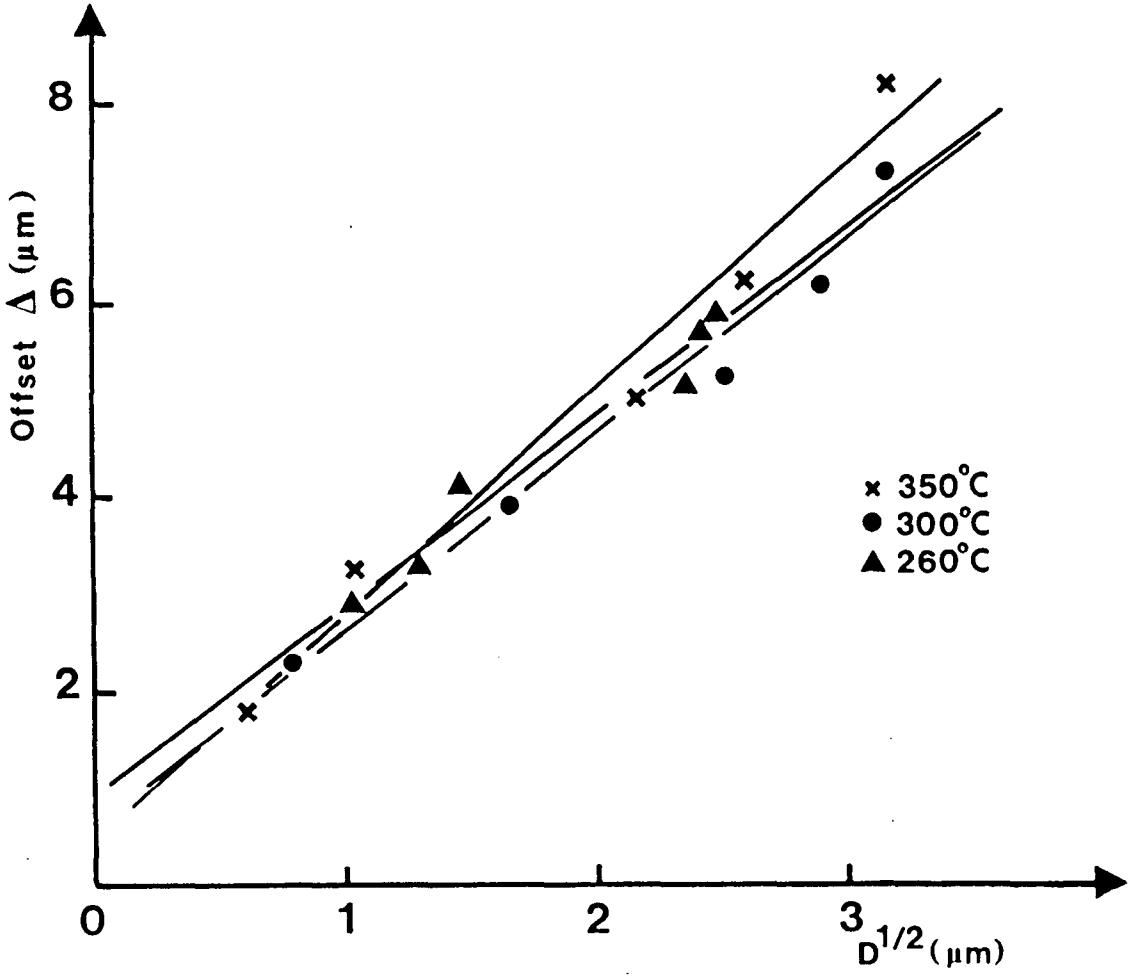

Morris - Mark - Morris

Fig 5a

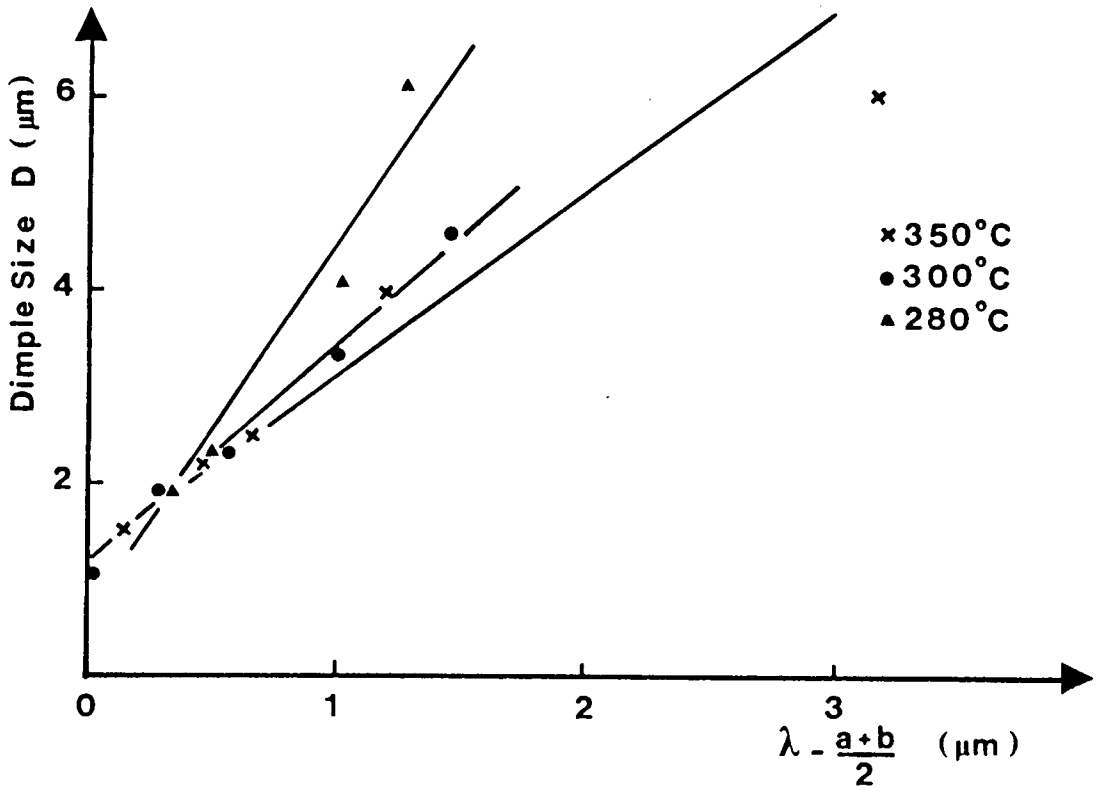

Morris - Mark - Morris

Fig 5b

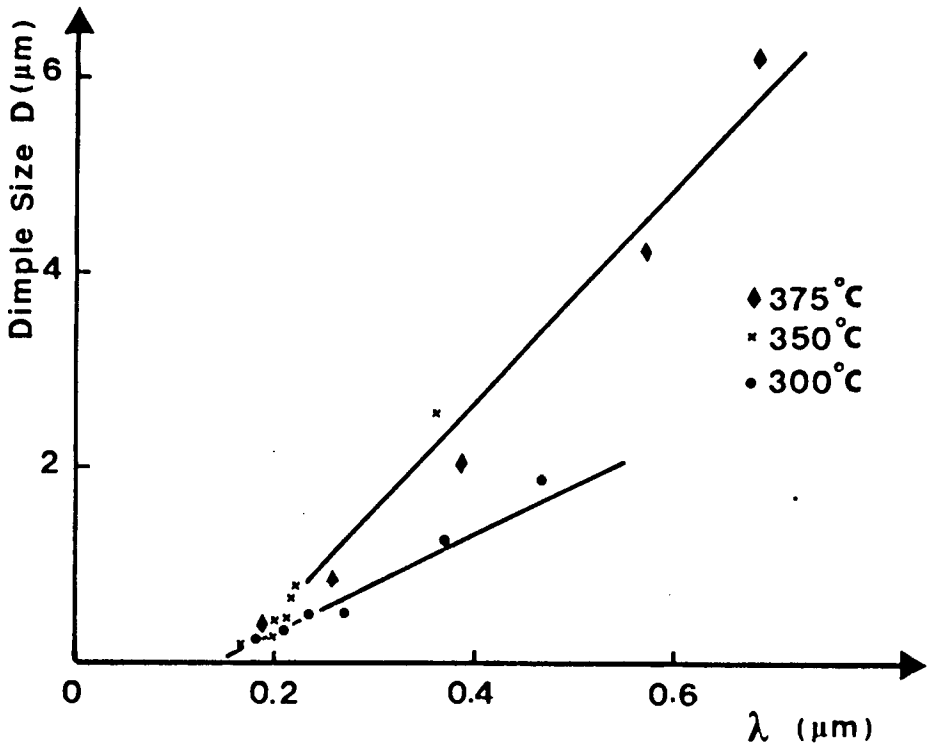

Morris Merle Morris

Fig 6a

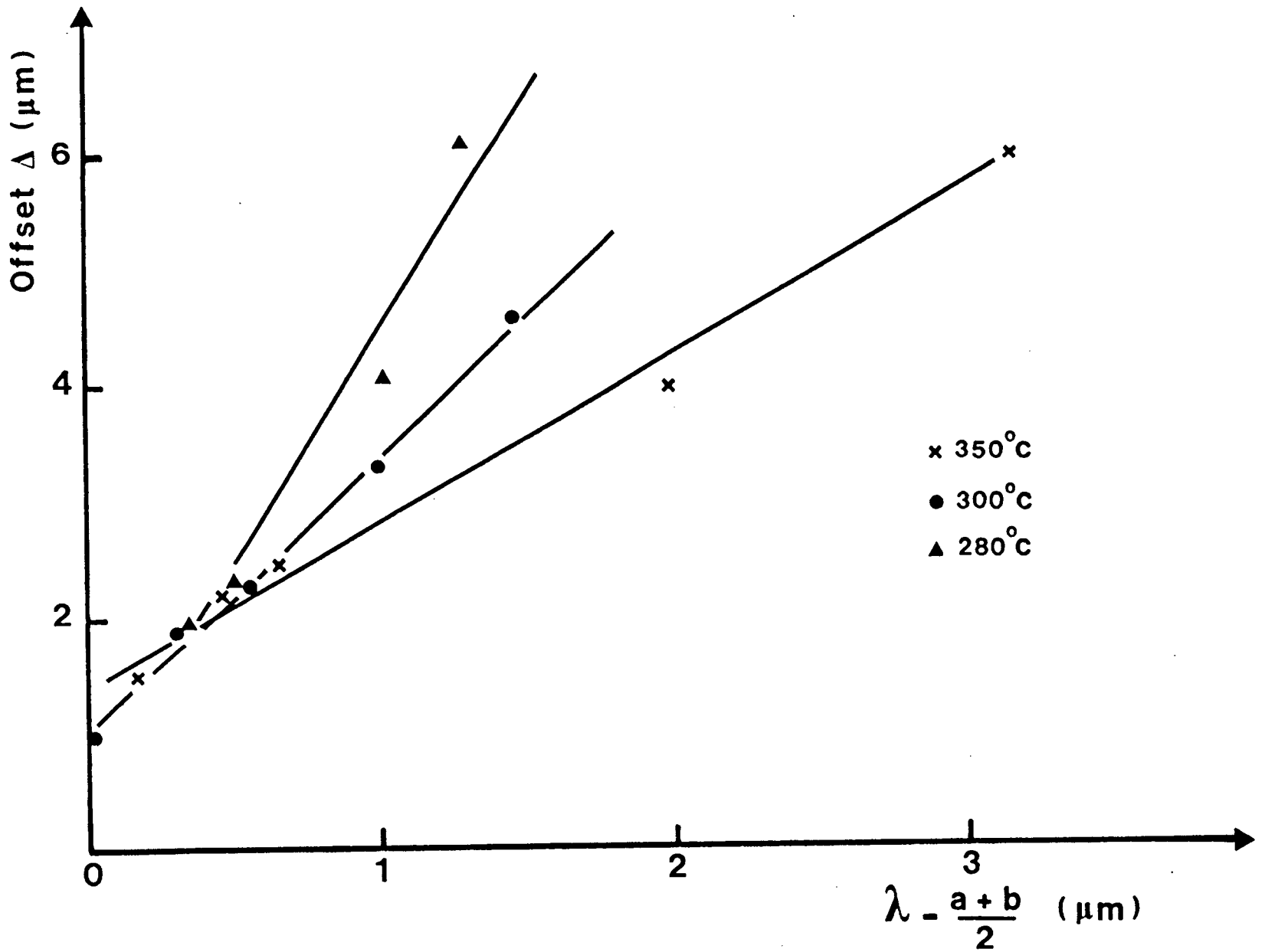

Morris - Merk - Morris

Fig 6b

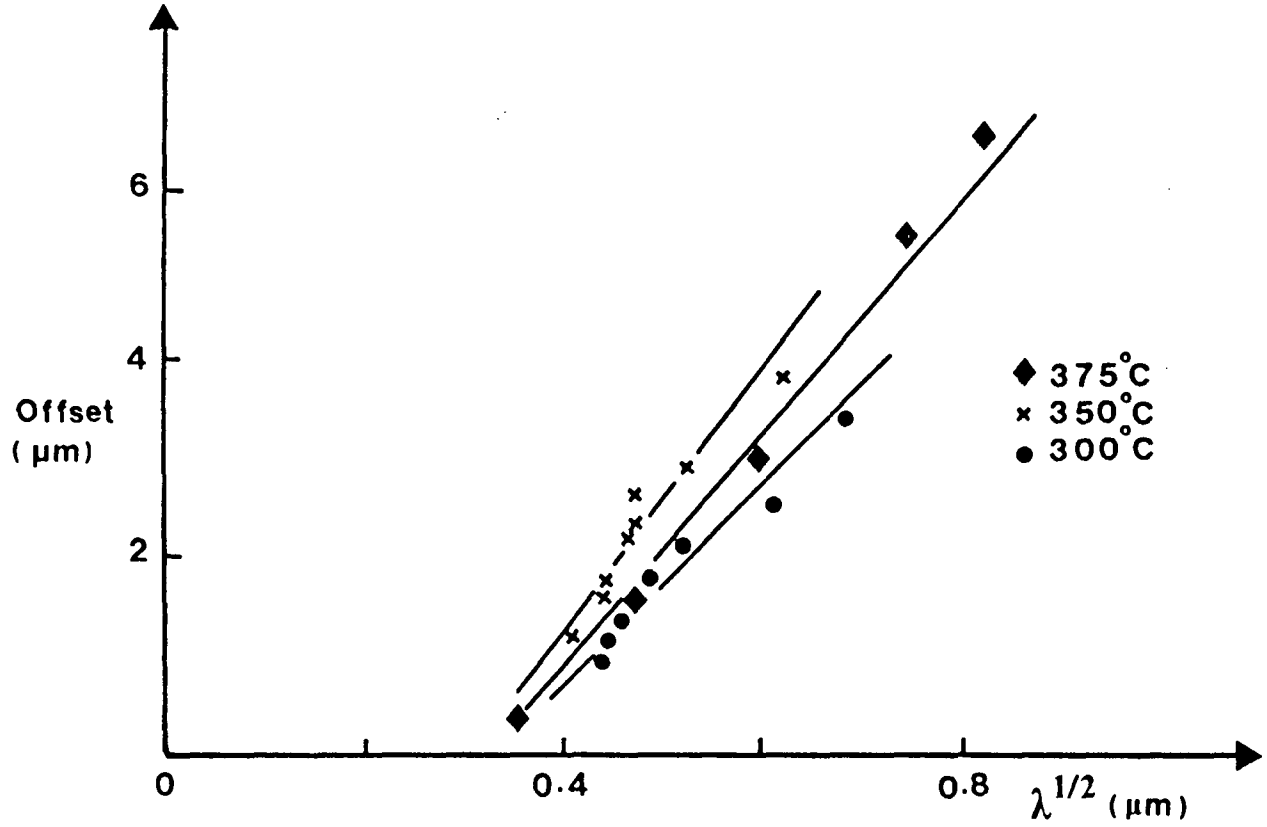

Mona-Herb-Mona

Fig 7.

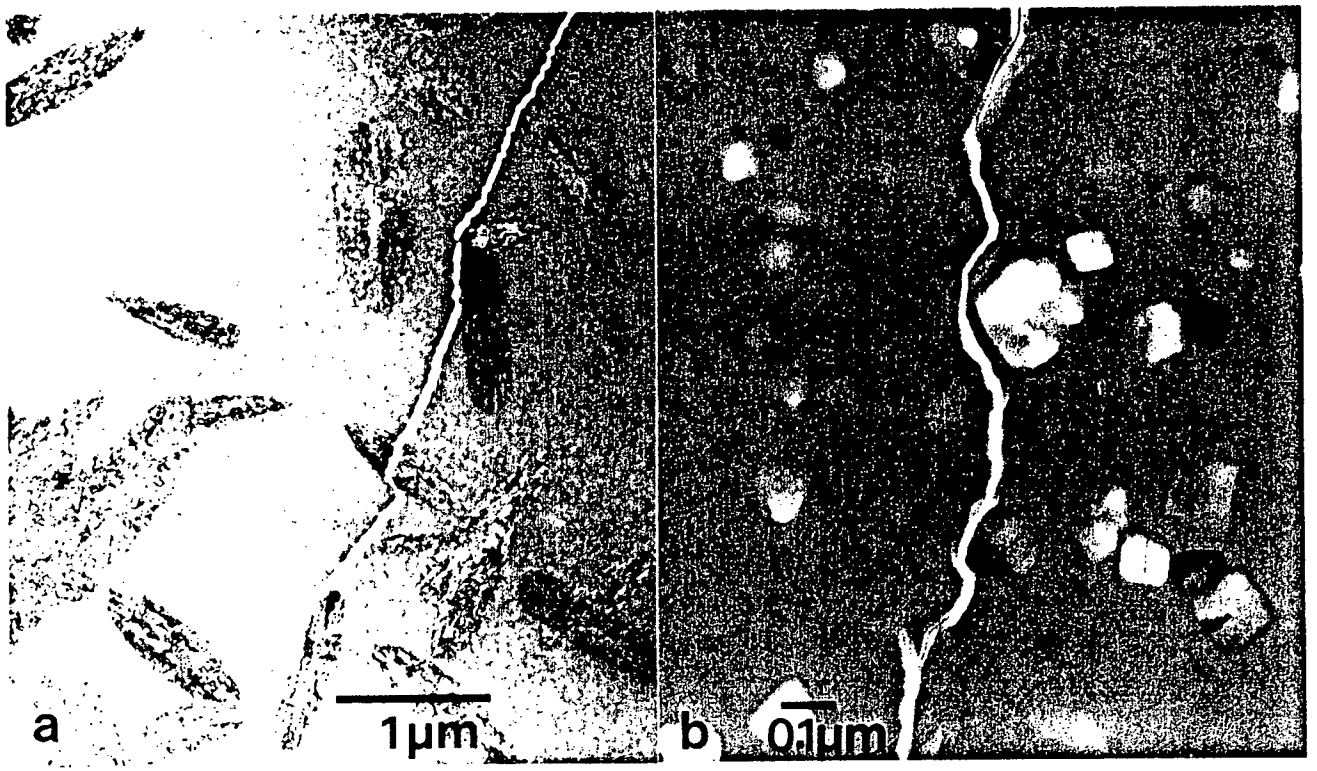

Morra - Merk - Morris

Fig 8

Fig 9. Morris - Mesh - Morris

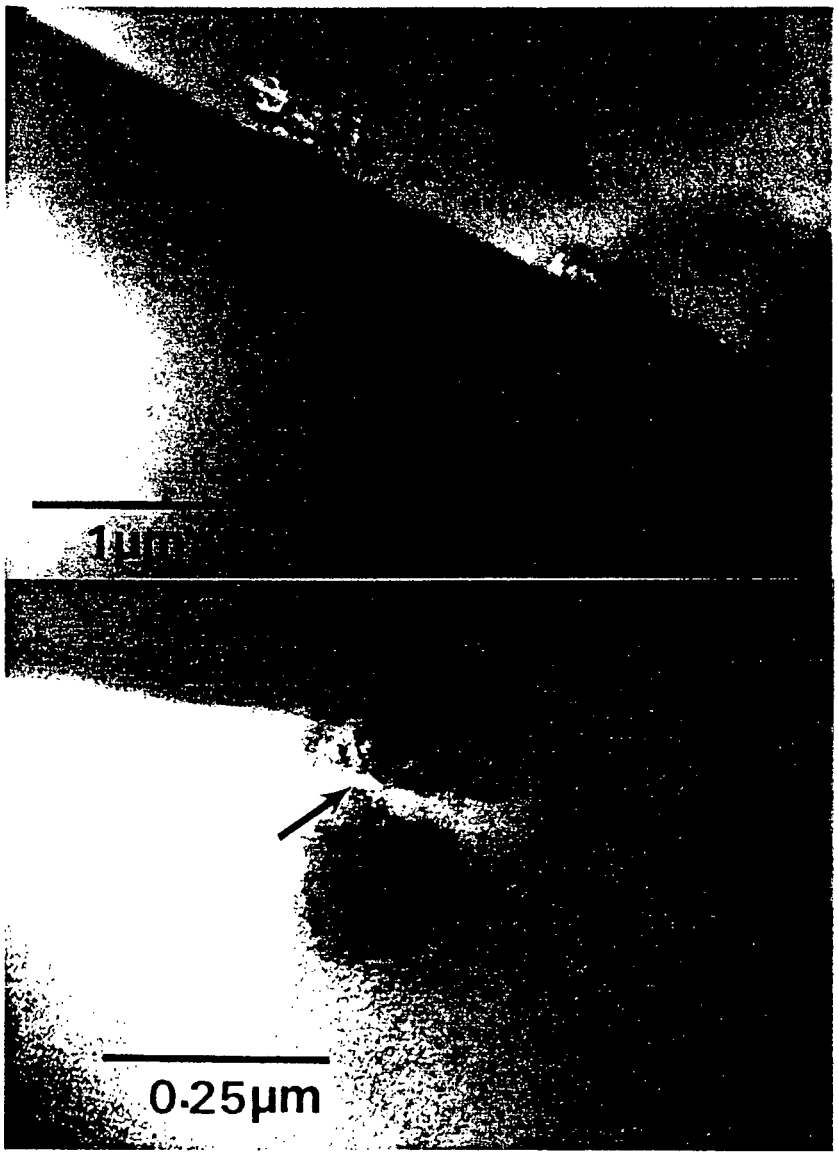

Fig 10 Mono-Meth-Mono

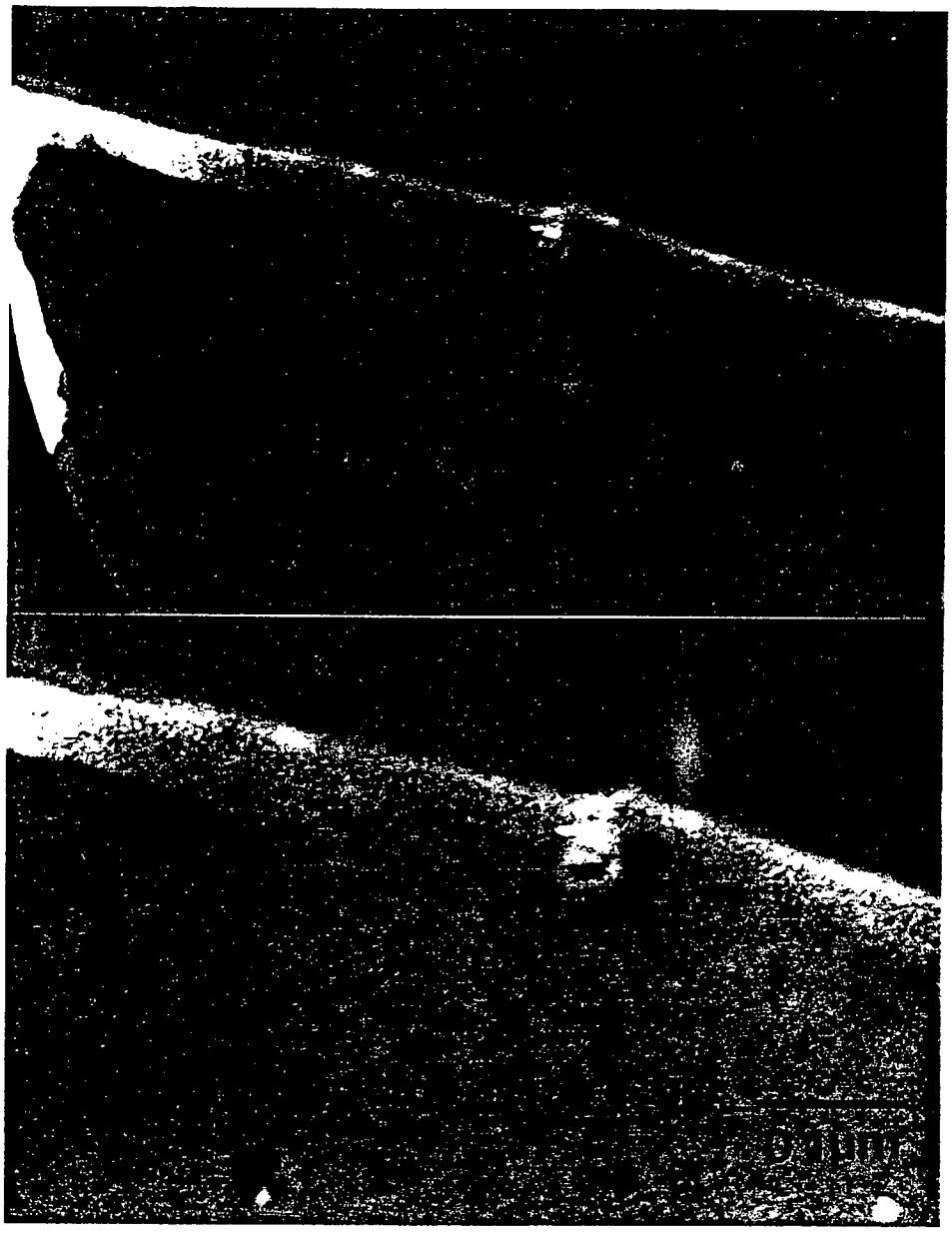

LISTE DE PUBLICATIONS:

- Crystallization Processes in Ni-Ti-B Glassy Alloys of Near-Ternary-Eutectic Composition. Acta Met. 35 (1987) 2213.

- Ductilisation and Embrittlement during the Crystallization of Ni-Ti-B Glasses. Submitted to J. Mat. Sci.

- Crystallization Embrittlement of Ni-Ti-B Glasses. Submitted to J. Mat. Sci.